Clinical and Translational Report

Cell Metabolism

Inosine Monophosphate Dehydrogenase Dependence in a Subset of Small Cell Lung Cancers

Graphical Abstract

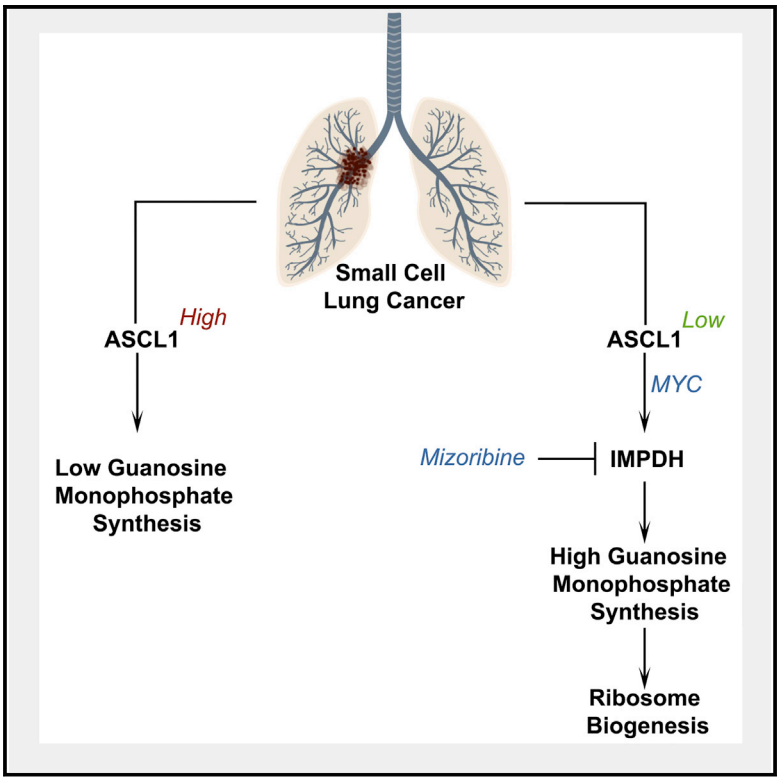

Authors

Fang Huang, Min Ni,
Milind D. Chalishazar, ...,
John D. Minna, Zeping Hu,
Ralph J. DeBerardinis

Correspondence

zeping_hu@mail.tsinghua.edu.cn (Z.H.),
ralph.deberardinis@
utsouthwestern.edu (R.J.D.)

In Brief

Huang et al. identify ASCL1-high and -low metabolic subtypes in small cell lung cancer (SCLC), linked to *de novo* guanosine nucleotide synthesis. Using a clinically available inhibitor of the purine biosynthetic pathway, they demonstrate reduced growth of ASCL1^{Low} SCLC tumors and favorable combination with chemotherapy in *in vivo* models.

Highlights

- Small cell lung cancers (SCLCs) are metabolically heterogeneous
- Levels of the lineage oncogene ASCL1 define metabolic groups of SCLC
- ASCL1^{Low} SCLCs have abundant purines, particularly guanosine nucleotides
- Inhibiting the guanosine synthetic enzyme IMPDH impairs ASCL1^{Low} tumor growth

Huang et al., 2018, Cell Metabolism *28*, 369–382
September 4, 2018
https://doi.org/10.1016/j.cmet.2018.06.005

CellPress

Cell Metabolism
Clinical and Translational Report

Inosine Monophosphate Dehydrogenase Dependence in a Subset of Small Cell Lung Cancers

Fang Huang,[1,2] Min Ni,[2] Milind D. Chalishazar,[3] Kenneth E. Huffman,[4] Jiyeon Kim,[2] Ling Cai,[2,5] Xiaolei Shi,[2] Feng Cai,[2] Lauren G. Zacharias,[2] Abbie S. Ireland,[3] Kailong Li,[2] Wen Gu,[2] Akash K. Kaushik,[2] Xin Liu,[2] Adi F. Gazdar,[4] Trudy G. Oliver,[3] John D. Minna,[4] Zeping Hu,[2,7,*] and Ralph J. DeBerardinis[2,6,8,*]

[1]Institute of Hematology, Union Hospital, Tongji Medical College, Huazhong University of Science and Technology, Wuhan, Hubei 430022, China
[2]Children's Medical Center Research Institute, University of Texas Southwestern Medical Center, Dallas, TX 75390, USA
[3]Department of Oncological Sciences, University of Utah, Huntsman Cancer Institute, Salt Lake City, UT 84112, USA
[4]Hamon Center for Therapeutic Oncology Research, University of Texas Southwestern Medical Center, Dallas, TX 75390, USA
[5]Department of Clinical Science, University of Texas Southwestern Medical Center, Dallas, TX 75390, USA
[6]Department of Pediatrics and Eugene McDermott Center for Human Growth and Development, University of Texas Southwestern Medical Center, Dallas, TX 75390, USA
[7]School of Pharmaceutical Sciences, Tsinghua University, Beijing 100084, China
[8]Lead Contact
*Correspondence: zeping_hu@mail.tsinghua.edu.cn (Z.H.), ralph.deberardinis@utsouthwestern.edu (R.J.D.)
https://doi.org/10.1016/j.cmet.2018.06.005

SUMMARY

Small cell lung cancer (SCLC) is a rapidly lethal disease with few therapeutic options. We studied metabolic heterogeneity in SCLC to identify subtype-selective vulnerabilities. Metabolomics in SCLC cell lines identified two groups correlating with high or low expression of the Achaete-scute homolog-1 (ASCL1) transcription factor (ASCL1^{High} and ASCL1^{Low}), a lineage oncogene. Guanosine nucleotides were elevated in ASCL1^{Low} cells and tumors from genetically engineered mice. ASCL1^{Low} tumors abundantly express the guanosine biosynthetic enzymes inosine monophosphate dehydrogenase-1 and -2 (IMPDH1 and IMPDH2). These enzymes are transcriptional targets of MYC, which is selectively overexpressed in ASCL1^{Low} SCLC. IMPDH inhibition reduced RNA polymerase I-dependent expression of pre-ribosomal RNA and potently suppressed ASCL1^{Low} cell growth in culture, selectively reduced growth of ASCL1^{Low} xenografts, and combined with chemotherapy to improve survival in genetic mouse models of ASCL1^{Low}/MYC^{High} SCLC. The data define an SCLC subtype-selective vulnerability related to dependence on *de novo* guanosine nucleotide synthesis.

INTRODUCTION

Neuroendocrine tumors account for about 20% of lung cancers, and most of these are small cell lung cancer (SCLC) (Govindan et al., 2006). Most SCLC patients have hematogenous metastases at the time of diagnosis and only a few (2%–5%) are candidates for surgery (Yu et al., 2010). Chemotherapy can palliate symptoms and prolong survival, but resistance emerges rapidly and long-term survival is rare (Demedts et al., 2010). Other than recent advances in immunotherapy, medical management of SCLC has changed little over several decades (Antonia et al., 2016). The National Cancer Institute Report to the United States Congress labeled SCLC as a "recalcitrant disease," and its dismal prognosis underscores the need for better understanding and advanced therapies (Minna and Rudin, 2014).

Most SCLCs express neuroendocrine markers including chromogranin A, neuron-specific enolase, neural cell adhesion molecule, and synaptophysin (Travis, 2010). These tumors are thought to arise from pulmonary neuroendocrine cells (Sutherland et al., 2011). ASCL1 is a critical transcription factor for neuroendocrine lineage development (a "lineage oncogene") and is required for tumor formation in some SCLC mouse models (Augustyn et al., 2014; Borromeo et al., 2016). High ASCL1 expression defines a major subset of human SCLC (ASCL1^{High}) with distinct gene expression and DNA methylation signatures (Borromeo et al., 2016; Poirier et al., 2015). A variant SCLC subset with low expression of neuroendocrine markers, including ASCL1, also exists in humans (George et al., 2015; Mollaoglu et al., 2017; Rekhtman, 2010). The lineage status of these ASCL1^{Low} tumors is unclear, but they often express the lineage factor NEUROD1 and exhibit sensitivity to oncolytic picornavirus (Poirier et al., 2013). *MYC* has been identified as a key driver of the ASCL1^{Low} SCLC subgroup with high NEUROD1 expression (Mollaoglu et al., 2017).

Over 90% of SCLCs, including both the ASCL1^{High} and ASCL1^{Low} subsets, contain mutations in *TP53* and *RB1*. Other frequent events include amplification of *NFIB*, *SOX2*, and genes encoding MYC family members (George et al., 2015; Peifer et al., 2012; Rudin et al., 2012). Genetically engineered mouse models (GEMMs) of SCLC are based on simultaneous deletion of *Tp53* and *Rb1* in the lung. This combination of mutations generates tumors with high penetrance but a long latency. Deletion of *Rbl2* or *Pten*, or overexpression of *Myc* together with deletion of *Tp53* and *Rb1*, accelerates SCLC tumorigenesis in mice (McFadden et al., 2014; Schaffer et al., 2010). Histological characterization

of SCLC GEMMs reveals that the *Rb1*$^{fl/fl}$*; p53*$^{fl/fl}$*; Rbl2*$^{fl/fl}$ (RPR2) and *Rb1*$^{fl/fl}$*; p53*$^{fl/fl}$*;Pten*$^{fl/fl}$ (RPP) tumors have neuroendocrine features and high ASCL1 expression, whereas *Rb1*$^{fl/fl}$*; p53*$^{fl/fl}$*; MycT58A*$^{LSL/LSL}$ (RPM) tumors have variant SCLC histology and low ASCL1 expression (Gazdar et al., 2015; Mollaoglu et al., 2017).

Because cancer cells rely on reprogrammed metabolism to support their survival and proliferation, characterization of reprogrammed activities might provide opportunities to inhibit tumor progression (Vander Heiden and DeBerardinis, 2017). Specific oncogenotypes produce distinct metabolic liabilities in some types of cancer (Boroughs and DeBerardinis, 2015; Hu et al., 2013; Li et al., 2014). Although non-small-cell lung cancer (NSCLC) is reported to have extensive metabolic heterogeneity in culture and *in vivo* (Hensley et al., 2016; Kim et al., 2017), little is known about metabolism in SCLC, including whether the molecular subsets have distinct metabolic preferences. We integrated data from metabolomic and transcriptomic profiling of SCLC cell lines and primary tumors from humans and mice to define a novel liability in ASCL1^{Low} tumors that can be targeted using clinically available inhibitors.

RESULTS AND DISCUSSION

Distinct Metabolomic Subsets of Human ASCL1^{High} and ASCL1^{Low} SCLC Cell Lines

We first assessed heterogeneity in SCLC by performing metabolomic and gene expression profiling in human SCLC cell lines. Non-negative matrix factorization clustering of gene expression in 29 cell lines revealed two major clusters, with ASCL1 as the top differential gene (Figures 1A and 1B). We designated these subtypes ASCL1^{High} and ASCL1^{Low}. Metabolomics in 26 of these cell lines revealed that the ASCL1^{High} and ASCL1^{Low} subtypes were fairly distinct on unsupervised clustering, although three groups were identified with a clade that is a mixture of high and low ASCL1 cells (Figures S1, S2A, and S2B). Supervised partial least-squares discriminant analysis and variable importance in the projection analysis revealed a set of metabolites that discriminated between the ASCL1^{High} and ASCL1^{Low} subtypes (Figure 1C). These included metabolites from pathways involving nucleotide biosynthesis, amino acid metabolism, and the tricarboxylic acid cycle. The ASCL1^{Low} group accumulated several purine nucleotides (Figure 1D). Purines provide essential intermediates for RNA and DNA synthesis, signaling, and energetics. The bases are synthesized *de novo* on 5-phosphoribosyl pyrophosphate or regenerated via base salvage from nucleotide degradation. Purine nucleotides detected in our metabolomic analysis, including inosine 5′-monophosphate (IMP), guanosine 5′-monophosphate (GMP), xanthosine 5′-monophosphate (XMP), and adenosine 5′-monophosphate (AMP), were significantly elevated in the ASCL1^{Low} group (Figure 1D). In contrast, pyrimidine metabolites were not consistently altered between the groups (Figure S2C). Metabolites from the methionine cycle were enriched in the ASCL1^{High} group (Figure 1D).

Purine *De Novo* Synthesis Genes Are Upregulated in ASCL1^{Low} SCLC

To obtain insights into the mechanism of purine accumulation in ASCL1^{Low} cells, we analyzed gene expression data from SCLC cell lines. Gene set enrichment analysis from two independent microarray datasets (Barretina et al., 2012; Byers et al., 2013) revealed significant enrichment of gene sets related to purine metabolism in ASCL1^{Low} SCLC cell lines (Figures S3A and S3B). Specifically, multiple genes involved in *de novo* purine synthesis had elevated expression in the ASCL1^{Low} group (Figure 2A).

IMP is an important intermediate in *de novo* purine biosynthesis because it can be converted to either GMP or AMP through two parallel pathways. Enzymes in the GMP pathway include IMPDH and GMP synthase (GMPS), and enzymes in the AMP pathway include adenylosuccinate synthase (ADSS) and adenylosuccinate lyase (ADSL). Whole-transcriptome correlation analysis using data from 51 SCLC cell lines in the Cancer Cell Line Encyclopedia (CCLE) identified genes for both IMPDH isoforms (IMPDH1 and IMPDH2), plus GMPS and ADSL as among the most inversely correlated with ASCL1 (Figure S3C). IMPDH catalyzes the conversion of IMP to XMP, the rate-limiting step of GMP synthesis. In our cell line panel, ASCL1^{Low} cells expressed high levels of IMPDH1 and IMPDH2 mRNA and protein (Figure 2B).

We next used a dataset of SCLC tumors from 81 patients (George et al., 2015) to ask whether ASCL1 correlates with expression of purine metabolic genes in primary human SCLC. Although primary tumors have more molecular heterogeneity than cell lines, non-negative matrix factorization clustering identified a distinct ASCL1^{Low} group accounting for about 20% of tumors in this cohort (cluster 4 in Figures 2C and 2D). Gene set enrichment analysis identified a purine metabolism signature in the ASCL1^{Low} cluster compared with all others (Figure 2E). As with ASCL1^{Low} cell lines, ASCL1^{Low} tumors overexpressed several purine synthesis genes, including *IMPDH1* and *IMPDH2* (Figure 2F). Purine salvage genes, in contrast, were not differentially expressed (Figure S3D).

ASCL1^{Low} SCLC Cell Lines Have High Rates of *De Novo* Purine Biosynthesis

Neither changes in metabolic gene expression nor changes in intracellular metabolites are sufficient to indicate changes in metabolic rates (Buescher et al., 2015). We therefore evaluated purine biosynthesis rates in SCLC cell lines by measuring incorporation of ^{15}N originating on [amide-^{15}N]glutamine into purine nucleotides as described by Ben-Sahra et al. (2016). In addition to the nitrogen contained in phosphoribosylamine, glutamine donates one additional amide nitrogen to IMP and two additional amide nitrogens to GMP (Figure 3A). As expected, IMP m+2, AMP m+2, and GMP m+3 were the dominant labeled forms of purines after culture with [amide-^{15}N]glutamine, and enrichment increased over time (Figure 3B). After 6 hr, ASCL1^{Low} cells showed higher fractions of IMP m+2, AMP m+2, and GMP m+3 than ASCL1^{High} cells (Figure 3C). Overall, ASCL1^{Low} cell lines tended to have somewhat higher rates of proliferation than ASCL1^{High} cell lines (Figure 3D), possibly contributing to the higher rates of purine synthesis. We also evaluated purine biosynthesis rates by measuring incorporation of ^{13}C arising on [U-^{13}C]glucose into purine nucleotides. ASCL1^{Low} cells had higher fractions of the m+5 and m+6 forms of GMP, AMP, and IMP at multiple time points compared with ASCL1^{High} cells (Figures 4A and 4B). Note that this analysis does not consider the higher purine abundance in ASCL1^{Low} cells, meaning that the

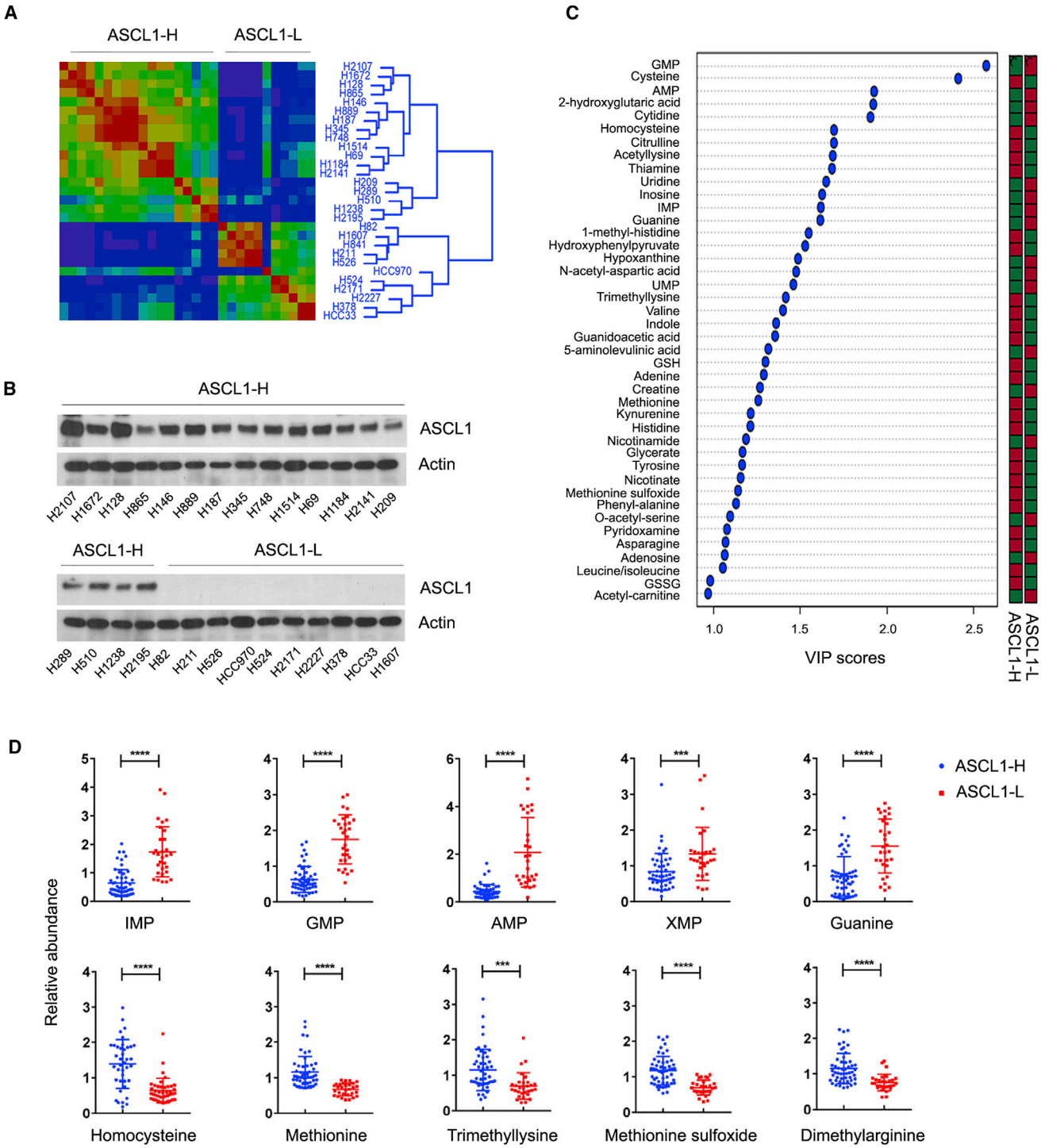

Figure 1. Distinct Metabolomic Subsets of Human SCLC Cell Lines

(A) Non-negative matrix factorization clustering of microarray gene expression shows two major clusters, designated as ASCL1^{High} and ASCL1^{Low} (ASCL1-H and ASCL1-L), in 29 SCLC lines. The ordered linkage tree demonstrates the relationship of gene expression patterns among these lines.

(B) ASCL1 abundance in 28 of the cell lines analyzed in (A).

(C) Metabolites discriminating between 13 ASCL1^{High} and 13 ASCL1^{Low} cell lines subjected to metabolomic profiling. These metabolites have variable importance in the projection (VIP) scores of 1.0 or higher. The bar on the right indicates whether each metabolite is enhanced (red) or depleted (green) in each class.

(D) Relative abundance of intermediates from purine and methionine metabolism in ASCL1^{High} and ASCL1^{Low} cell lines. Individual data points are shown along with mean abundance values and SD for three independent cultures of each line. ***$p < 0.001$, ****$p < 0.0001$.

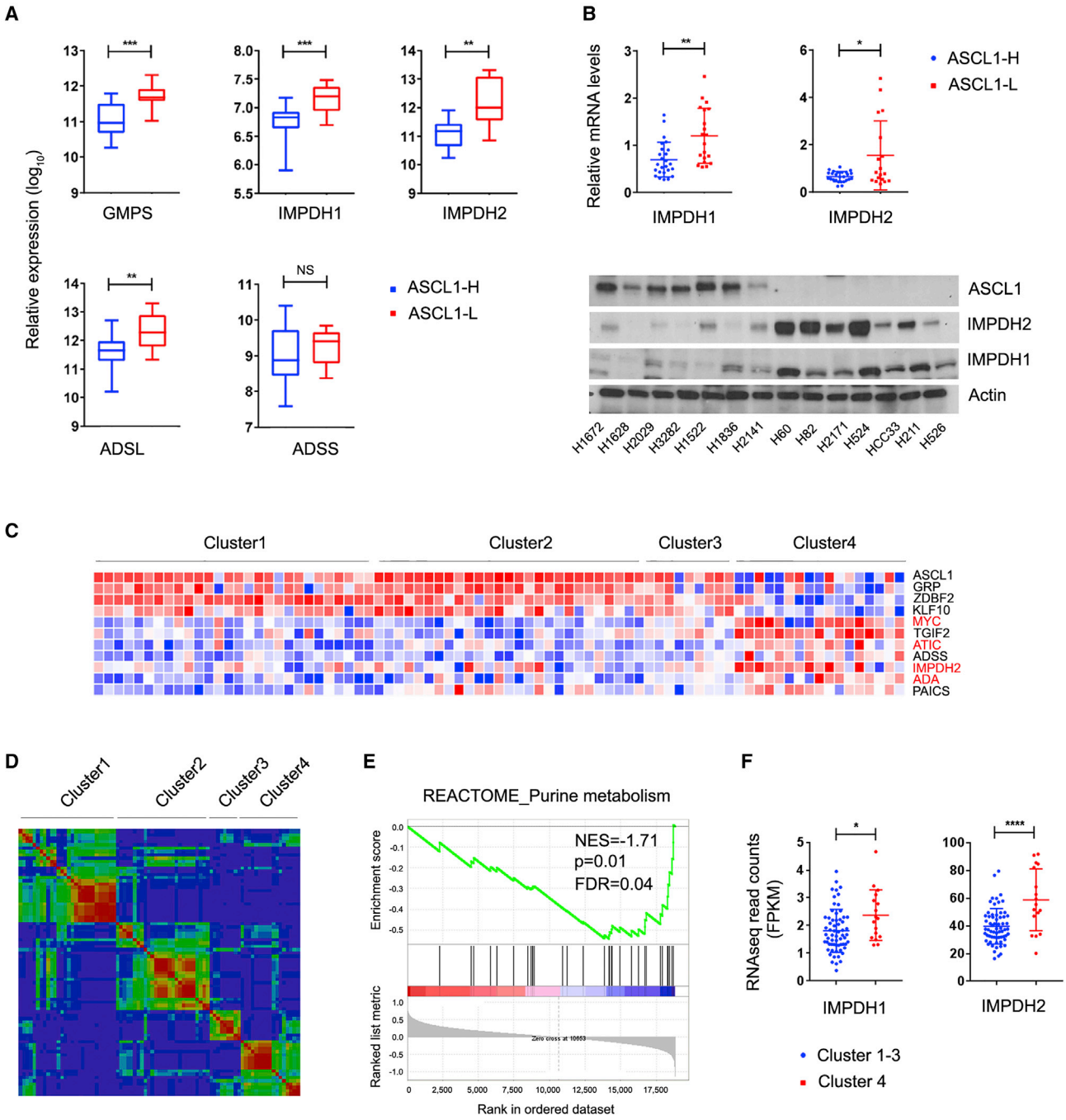

Figure 2. Enhanced Expression of Enzymes Involved in Purine Biosynthesis in ASCL1^{Low} SCLC

(A) Relative mRNA abundance of genes involved in purine metabolism. ASCL1^{High} and ASCL1^{Low} SCLC cell lines from Figure 1A were used in the analysis. **p < 0.01; ***p < 0.001.

(B) Relative mRNA and protein abundance of IMPDH1 and IMPDH2 in seven ASCL1^{High} and seven ASCL1^{Low} cell lines. Individual data points are shown together with mean and SD for three independent cultures of each line. *p < 0.05; **p < 0.01.

(C and D) Heatmap and non-negative matrix factorization clustering of RNA-seq gene expression data from 81 SCLC primary tumors. Cluster 4 corresponds to the ASCL1^{Low} subset. The heatmap highlights representative transcripts including *MYC* and several purine metabolic genes (in red).

(E) Gene set enrichment analysis reveals enrichment of the "REACTOME_purine metabolism" gene set in cluster 4 compared with the other three clusters in (D).

(F) Relative mRNA abundance of *IMPDH1* and *IMPDH2* in clusters 1–3 versus cluster 4 tumors. Individual data points are shown together with means and SD for each sample. *p < 0.05; ****p <0.0001.

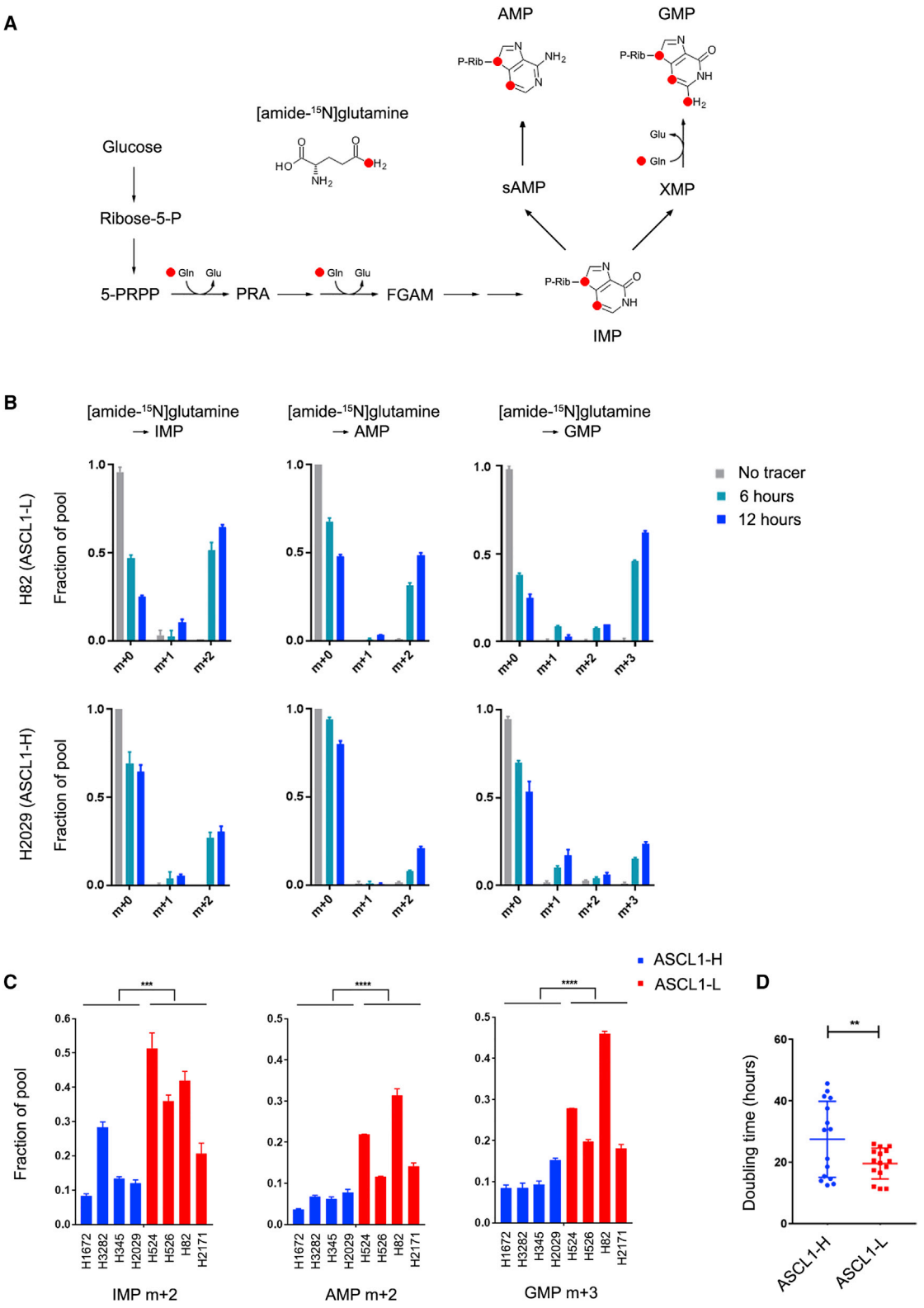

Figure 3. ASCL1^{Low} SCLC Cell Lines Have High Rates of *De Novo* Purine Biosynthesis

(A) Schematic of *de novo* purine synthesis, illustrating labeling from [amide-^{15}N]glutamine.

(B) Fractional labeling of IMP, GMP, and AMP in H82 cells (ASCL1^{Low}) and H2029 cells (ASCL1^{High}) with [amide-^{15}N]glutamine for 6 or 12 hr. "No tracer" indicates the mass distribution of cells cultured with unlabeled glutamine. Data are the average and SD of three cultures.

(legend continued on next page)

true flux is likely underestimated. Taken together, these data show that *de novo* purine synthesis is enhanced in ASCL1^{Low} SCLC cells.

MYC Regulates *De Novo* Purine Nucleotide Synthesis in ASCL1^{Low} SCLC Lines

To define the mechanism for enhanced purine synthesis in ASCL1^{Low} SCLC, we again analyzed mRNA expression from the cohort of 81 SCLC primary tumors. Whole-transcriptome correlation analysis ranked *MYC* as one of the most inversely correlated genes with ASCL1; only 69 of 28,660 transcripts had lower correlation coefficients (Figure S4A), consistent with the finding that overexpression of *Myc* induces formation of ASCL1^{Low} SCLC in mice (Mollaoglu et al., 2017). *MYC* mRNA and protein levels were also enhanced in ASCL1^{Low} SCLC cell lines (Figures 5A and 5B). In other forms of cancer, MYC regulates purine biosynthesis in part through transcriptional activation of *IMPDH1* and *IMPDH2* (Liu et al., 2008; Stine et al., 2015). In the CCLE gene expression database, *MYC* correlates highly with expression of *IMPDH1*, *IMPDH2*, and *GMPS* in SCLC cell lines (Figure S4B). Furthermore, published chromatin immunoprecipitation followed by sequencing (ChIP-seq) data (GEO: GSM894102) (Lin et al., 2012) of the *IMPDH1* and *IMPDH2* loci in H2171 (ASCL1^{Low}) cells revealed MYC binding at the promoter regions of both genes (Figure S4C). ChIP-seq experiments did not localize ASCL1 to the promoters of *MYC*, *IMPDH1*, or *IMPDH2* in H2107 (ASCL1^{High}) cells (Figure S4E). Forced ASCL1 overexpression did not markedly change the expression of MYC or IMPDH2, although IMPDH1 expression decreased somewhat (Figure S4F). Although ChIP-seq data in H2171 cells showed MYC binding at the *ASCL1* promoter region (Figure S4E), forced MYC overexpression did not change the expression of ASCL1, and CRISPR/Cas9-mediated *MYC* knockout in H82 (ASCL1^{Low}) cells did not induce ASCL1 expression (Figure S4F). We scanned the promoter region of *IMPDH2* using the JASPAR database and identified three typical E boxes overlapping with the ChIP-seq binding area of MYC (Figure S4G). Luciferase reporter assays revealed that the wild-type *IMPDH2* promoter generated substantial luciferase activity while deletion of the three E boxes markedly attenuated luciferase activity (Figure S4G).

MYC knockout in H82 (ASCL1^{Low}) cells nearly eliminated expression of both IMPDH1 and IMPDH2 mRNA and protein (Figure 5C). MYC deficiency also reduced the flow of ^{15}N from [amide-^{15}N]glutamine into GMP m+3 and AMP m+2, although these cells were still capable of producing IMP m+2 upstream of IMPDH (Figure 5D). Taken together, these data demonstrate that MYC enhances *de novo* purine nucleotide synthesis through transcriptional regulation of biosynthetic genes in ASCL1^{Low} cells.

Enhanced Expression of the GMP Synthesis Pathway in a Mouse Model of ASCL1^{Low} SCLC

Transgenic *Myc^{T58A}* expression drives a variant subset of ASCL1^{Low} SCLC with low neuroendocrine features in tumors that also harbor deletions of *Rb1* and *Tp53* (RPM mice) (Mollaoglu et al., 2017). To investigate *de novo* purine synthesis in GEMMs of SCLC, we compared primary tumors from RPM (ASCL1^{Low}) mice with RPP and RPR2 (ASCL1^{High}) mice. IMPDH1, IMPDH2, and GMPS were more abundantly expressed at the mRNA (Figure 5E) and protein (Figure 5F) levels in RPM tumors than in the other genotypes. XMP and GMP were also elevated in RPM tumors (Figure 5G). ChIP-seq data of the *Impdh1* and *Impdh2* loci in RPM tumors indicated MYC binding at both promoters, further validating the regulation of GMP synthesis by MYC in ASCL1^{Low} SCLC (Figure S4D).

IMPDH Is a Druggable Target and Selectively Inhibits ASCL1^{Low} SCLC Cell and Tumor Growth

To investigate the requirement for *de novo* GMP biosynthesis in ASCL1^{Low} SCLC, we determined IC_{50} values for the IMPDH inhibitor mycophenolic acid (MPA) in a panel of SCLC cell lines. MPA more potently suppressed growth of ASCL1^{Low} than ASCL1^{High} cells (Figure 6A). This was not due to an overall enhanced sensitivity of ASCL1^{Low} cells to metabolic inhibitors, as ASCL1^{High} cell lines were more sensitive to cycloleucine, an inhibitor of methyladenosine transferase (MAT) in the methionine cycle, and the thymidylate synthase inhibitor 5-fluorouracil had similar efficacy between the two classes (Figure 6A). CRISPR/Cas9-mediated *IMPDH1* knockout also reduced the viability of ASCL1^{Low} cells, but not ASCL1^{High} cells, while MAT2A knockout was selectively toxic to ASCL1^{High} cells (Figures 6B and S5A). MPA's toxicity was reversed by supplementing the cells with guanosine, indicating that the mechanism of action was through depletion of guanosine (Figure 6C). Moreover, metabolomics revealed that MPA resulted in accumulation of IMP and AICAR (5-aminoimidazole-4-carboxamide ribonucleotide), depletion of XMP and GMP, and no changes in AMP, all consistent with the intended inhibition of IMPDH (Figure 6D). These perturbations were more prominent in ASCL1^{Low} cells than ASCL1^{High} cells, consistent with the elevated IMPDH activity in the former (Figure S5B). Longer-term treatment of ASCL1^{Low} cells with MPA essentially eliminated colony formation in soft agar (Figure S5C).

MYC regulates ribosome biogenesis in many cancer cells (Devlin et al., 2016; Koh et al., 2011; Pozzo et al., 2017; Sabo et al., 2014), and we observed mRNAs involved in this pathway to be enriched in ASCL1^{Low} SCLC lines and RPM tumors (Figures S5D and S5E). Transcription of ribosomal RNAs by RNA polymerase I (Pol I) is the rate-limiting step in ribosome biogenesis, raising the possibility that production of these RNAs might be specifically suppressed after purine synthesis inhibition in ASCL1^{Low} SCLC cells with high MYC expression. Examining

(C) Fractional labeling of IMP, GMP, and AMP in four ASCL1^{High} and four ASCL1^{Low} lines cultured in medium containing [amide-^{15}N]glutamine for 6 hr. Data are the average and SD of three cultures. ***$p < 0.001$, ****$p < 0.0001$.

(D) Doubling time of five ASCL1^{High} and five ASCL1^{Low} lines, including all eight subjected to isotope labeling. Each cell line was cultured in triplicate to determine doubling time. Individual data points are shown together with the mean and SD. **$p < 0.01$.

Ribose-5-P, ribose 5-phosphate; 5-PRPP, 5-phosphoribosyl pyrophosphate; PRA, 5-phosphoribosylamine; FGAM, 5′-phosphoribosylformylglycinamidine; IMP, inosine 5′-monophosphate; XMP, xanthosine 5′-monophosphate; GMP, guanosine 5′-monophosphate; sAMP, adenylosuccinate; AMP, adenosine 5′-monophosphate; Gln, glutamine; Glu, glutamate; Asp, aspartate.

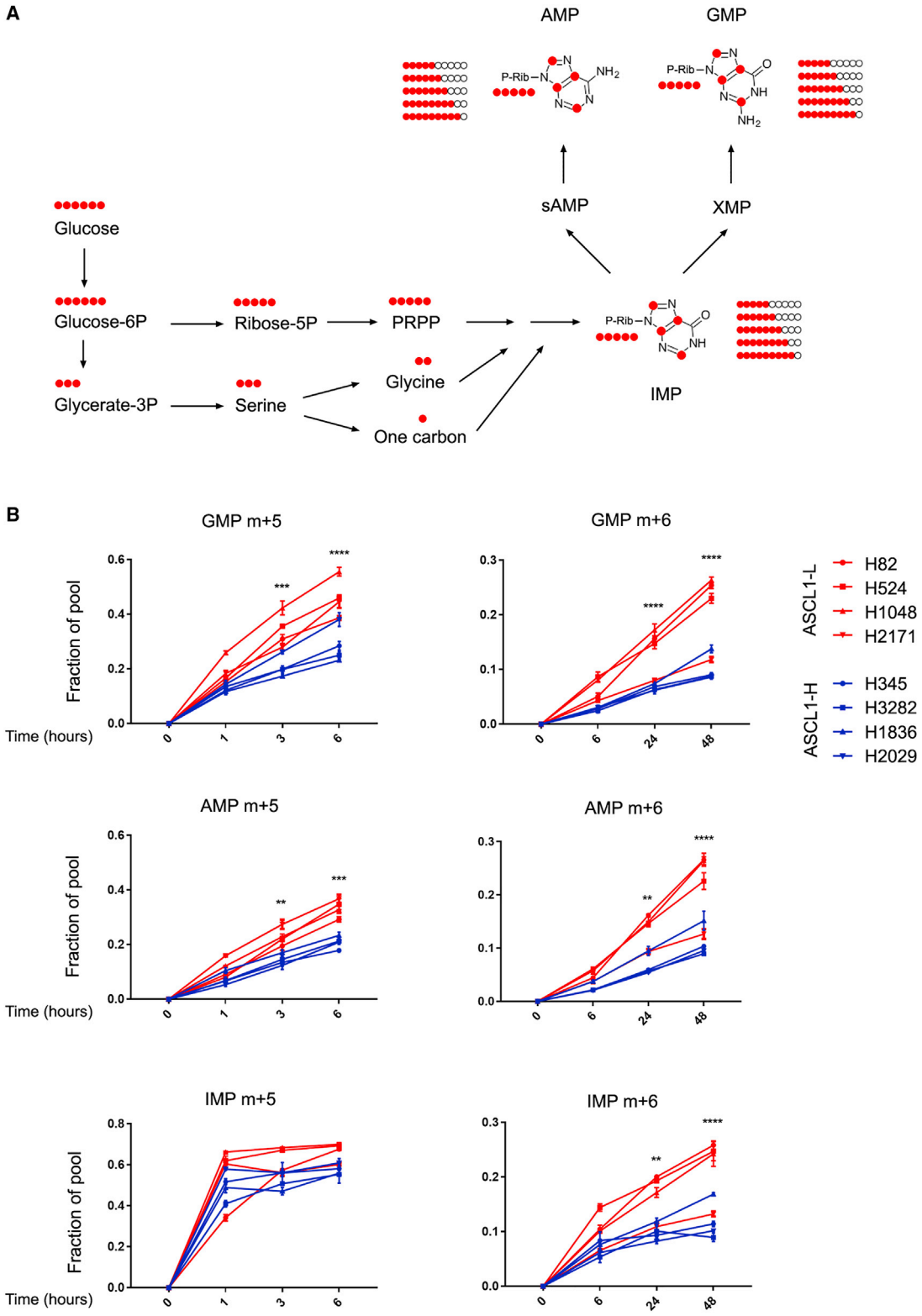

Figure 4. ASCL1^{Low} SCLC Cell Lines Have High Rates of *De Novo* Purine Biosynthesis

(A) Schematic of *de novo* purine synthesis, illustrating labeling from [U-^{13}C]glucose.

(B) Fractional labeling of IMP, GMP, and AMP in four ASCL1^{High} and four ASCL1^{Low} lines cultured in medium containing [U-^{13}C]glucose for 1, 3, 6, 24, and 48 hr. Data are the average and SD of three cultures. The m+5 and m+6 isotopologs were the two most prominent labeled forms of these purines. **$p < 0.01$; ***$p < 0.001$; ****$p < 0.0001$.

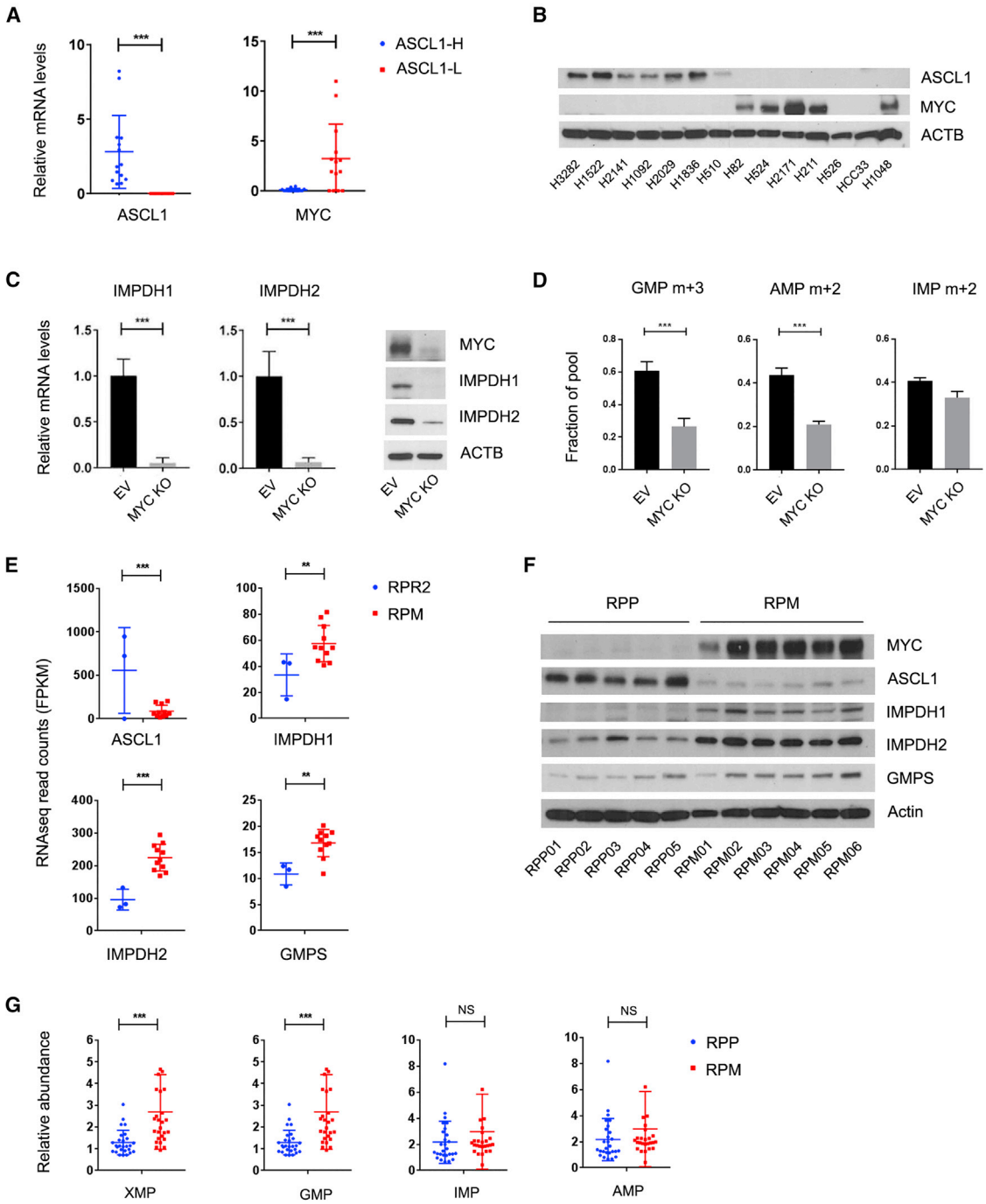

Figure 5. MYC Regulates *De Novo* Purine Nucleotide Synthesis in ASCL1^{Low} SCLC

(A and B) Relative abundance of ASCL1 and MYC mRNA and protein in seven ASCL1^{High} and seven ASCL1^{Low} cell lines. Individual data points are shown along with mean abundance values and SD for two independent cultures of each line. ***$p < 0.001$.

(C) Relative abundance of IMPDH1 and IMPDH2 mRNA and protein in ASCL1^{Low} H82 cells after CRISPR/Cas9-mediated *MYC* knockout (MYC KO). Data are represented as averages and SD. ***$p < 0.001$.

(D) Fractional labeling of GMP and IMP in empty vector control (EV) and MYC KO H82 cells after 4 hr of labeling in medium containing [amide-^{15}N]glutamine. Data are the average and SD of three cultures. ***$p < 0.001$.

(E) Relative mRNA abundance of *Ascl1*, *Impdh1*, *Impdh2*, and *Gmps* in RPR2 and RPM tumors. Individual data points are shown together with the mean and SD for each sample. Gene expression data from GEO: GSE89660. **$p < 0.01$; ***$p < 0.001$.

(F) Protein abundance of MYC, ASCL1, IMPDH1, IMPDH2, and GMPS in RPP and RPM tumors.

(G) Relative abundance of purine intermediates in RPP and RPM tumors. Individual data points are shown together with means and SD for three independent tumor fragments from nine mice in each group. ***$p < 0.001$.

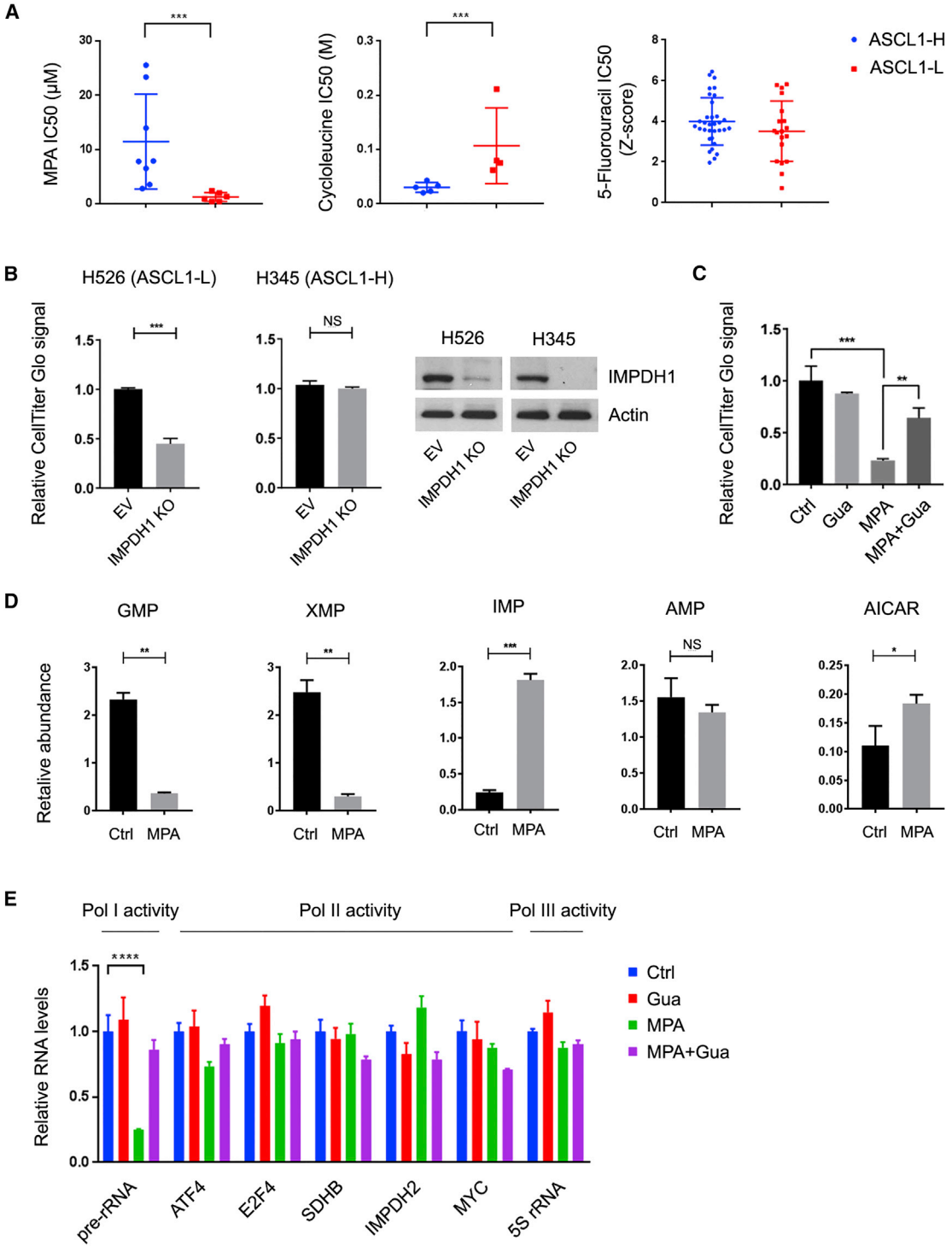

Figure 6. IMPDH Is Required for ASCL1^{Low} SCLC Cell Growth

(A) IC_{50} of IMPDH inhibitor MPA, MAT inhibitor cycloleucine, and 5-fluorouracil in ASCL1^{High} and ASCL1^{Low} cells. Individual data points are shown together with mean and SD of 14 lines for MPA and 10 lines for cycloleucine. Sensitivity of 60 cell lines to 5-fluorouracil is from the Genomics of Drug Sensitivity in Cancer database. ***$p < 0.001$.

(B) Relative growth of H345 (ASCL1^{High}) and H526 (ASCL1^{Low}) cells upon CRISPR/Cas9-mediated *IMPDH1* knockout. Data are represented as averages and SD. ***$p < 0.001$.

(C) Relative growth of H526 (ASCL1^{Low}) cells treated with 1 μM MPA with or without 50 μM guanosine for 72 hr. Data are represented as averages and SD. **$p < 0.01$; ***$p < 0.001$.

(legend continued on next page)

the abundance of selected transcripts from Pol I, II, and III revealed selective reduction of Pol I transcripts after 12 hr of treatment with MPA, and this suppression was completely reversed by guanosine (Figures 6E and S6A). These findings indicate that IMPDH enzymes are required to maintain levels of ribosomal RNAs in ASCL1^{Low} SCLC cells. Over the same period, effects on cell-cycle distribution and DNA content were marginal, arguing against DNA synthesis as a major factor in at least the early phase of MPA sensitivity (Figure S6B). MPA induced apoptosis after 48 hr, and this effect was also reversed by guanosine (Figures S6C and S6D). MPA did not induce senescence under these conditions (Figure S6E).

Because mammalian target of rapamycin complex 1 (mTORC1) signaling can enhance sensitivity to IMPDH inhibition (Valvezan et al., 2017), we examined the contribution of this pathway to MPA sensitivity in ASCL1^{Low} SCLC cells. Reverse-phase proteomics array data from 24 SCLC cell lines showed no significant difference in indicators of mTORC1 activity between ASCL1^{High} and ASCL1^{Low} cells (Figure S7A). We also validated by western blot that the abundance of p-4EBP1 (T37/46), p-p70S6K (T389), and p-S6 (S235/236), all of which reflect mTORC1 activity, did not systematically differ between ASCL1^{High} and ASCL1^{Low} cells (Figure S7B). Furthermore, inhibiting mTORC1 with Torin-1 did not alter the abundance of IMPDH1 or IMPDH2 or sensitivity to MPA (Figures S7C and S7D). These data suggest that in SCLC cells, MYC rather than mTORC1 is the key factor determining the need for guanosine synthesis. In further support of this model, ectopic MYC expression in ASCL1^{High} cells enhances MPA sensitivity (Figures S7E and S7F), indicating that MYC is sufficient to addict cells to IMPDH.

To test the *in vivo* efficacy of IMPDH inhibition, we injected non-obese diabetic/severe combined immunodeficient interleukin-2 receptor-γ chain null (NSG) mice subcutaneously with two ASCL1^{High} and two ASCL1^{Low} lines and treated with the IMPDH inhibitor mizoribine when palpable tumors were present. These experiments used mizoribine rather than MPA because of mizoribine's superior biodistribution *in vivo* (Koehl et al., 2007). Mizoribine is phosphorylated *in vivo* to the active drug mizoribine-5-monophosphate, which inhibits IMPDH activity with a K_i of 10^{-8} M (Ishikawa, 1999). Mizoribine was administered intraperitoneally (100 mg/kg) every other day for 2–3 weeks. Compared with vehicle control, mizoribine attenuated growth of both ASCL1^{Low} tumor lines, but neither of the ASCL1^{High} tumor lines (Figure 7A). Metabolite analysis of H524 (ASCL1^{Low}) tumors harvested after 2 weeks of mizoribine treatment revealed depletion of XMP and accumulation of IMP, consistent with *in vivo* IMPDH inhibition (Figure 7B).

Finally, to assess mizoribine's efficacy in GEMMs with autochthonous SCLC and an intact immune system, we used RPM mice. In this model of aggressive SCLC, cytotoxic chemotherapy combines with targeted agents to prolong survival (Mollaoglu et al., 2017). IMPDH inhibition rapidly depletes rRNA, suggesting that it may provide additive or synergistic effects when combined with drugs targeting DNA replication or damage. We determined that the combination indices of IMPDH inhibition with either cisplatin or etoposide were approximately 1.0 in culture, indicating an additive effect (Figure S7G). We established a cohort of RPM mice to determine mizoribine's efficacy as a single agent or in combination with cisplatin and etoposide. When tumor burden reached 10%–12% of the total pulmonary volume, mice were randomized to treatment with vehicle, mizoribine alone (100 mg/kg every other day), chemotherapy alone (5 mg/kg cisplatin and 10 mg/kg etoposide once a week), or mizoribine plus chemotherapy. Mice were euthanized when they developed labored respiration due to pulmonary tumor burden. Mizoribine monotherapy enhanced survival over vehicle by about 3 days, less than the effect of chemotherapy alone (Figure 7C). However, combining mizoribine and chemotherapy provided by far the most significant benefit in both survival and reduced tumor burden (Figures 7C and 7D).

Perspective

Metabolic phenotyping can uncover genotype-specific liabilities in NSCLC (Kim et al., 2013, 2017; Liu et al., 2013), but little is known about metabolic heterogeneity in SCLC and its relationship to molecular subclasses or therapeutic vulnerabilities. Although we observed that each SCLC cell line in our study has a unique metabolomic fingerprint, clustering of metabolic phenotypes revealed two major classes that largely correlated with the molecular subgroups defined by ASCL1. Metabolites from multiple pathways were among those that discriminate between the families, with metabolites from purine metabolism (up in ASCL1^{Low}) and methylation-related pathways (down in ASCL1^{Low}) being prominently featured. Because all cell lines were cultivated under identical conditions, these differences reflect cell-intrinsic metabolic preferences. It is intriguing to speculate that these preferences are related to the distinct developmental lineages observed in ASCL1^{Low} and ASCL1^{High} SCLC. ASCL1^{High} SCLCs express typical markers of the neuroendocrine lineage, whereas ASCL1^{Low} SCLCs are less differentiated, have less clear lineage, and tend to be aggressive with a high risk of metastasis in humans and mice (Gazdar et al., 1985; Johnson et al., 1992; Mollaoglu et al., 2017). The intense growth of these tumors *in vivo* may underlie their need for high rates of *de novo* guanosine nucleotide synthesis and ribosomal biogenesis.

The phenotype of enhanced purine metabolism in ASCL1^{Low} SCLC is related to the high levels of MYC expression in most cells/tumors from this molecular class. MYC regulates purine biosynthesis in part by activating transcription of *IMPDH1* and *IMPDH2*, as previously reported in other cell lines (Koh et al., 2011; Mannava et al., 2008; Pozzo et al., 2017; Sabo et al., 2014). MYC is exquisitely anti-correlated with ASCL1 expression in human SCLC, and we find that MYC correlates with the expression of IMPDH1 and IMPDH2 in SCLC tumors and cells derived from both humans and mice. We also find that flux through the IMPDH1/2-dependent pathway of guanosine nucleotide synthesis is MYC dependent in ASCL1^{Low} SCLC cells.

(D) Purine metabolite abundance in H524 (ASCL1^{Low}) cells treated with 1 μM MPA for 12 hr. Data are represented as averages and SD. *$p < 0.05$; **$p < 0.01$; ***$p < 0.001$.

(E) qPCR for transcripts of pre-rRNA, *ATF4*, *E2F4*, *SDHB*, *IMPDH2*, *MYC*, and 5S rRNA in H524 cells treated with 1 μM MPA with or without 50 μM guanosine for 12 hr. ****$p < 0.0001$. Data are represented as averages and SEM.

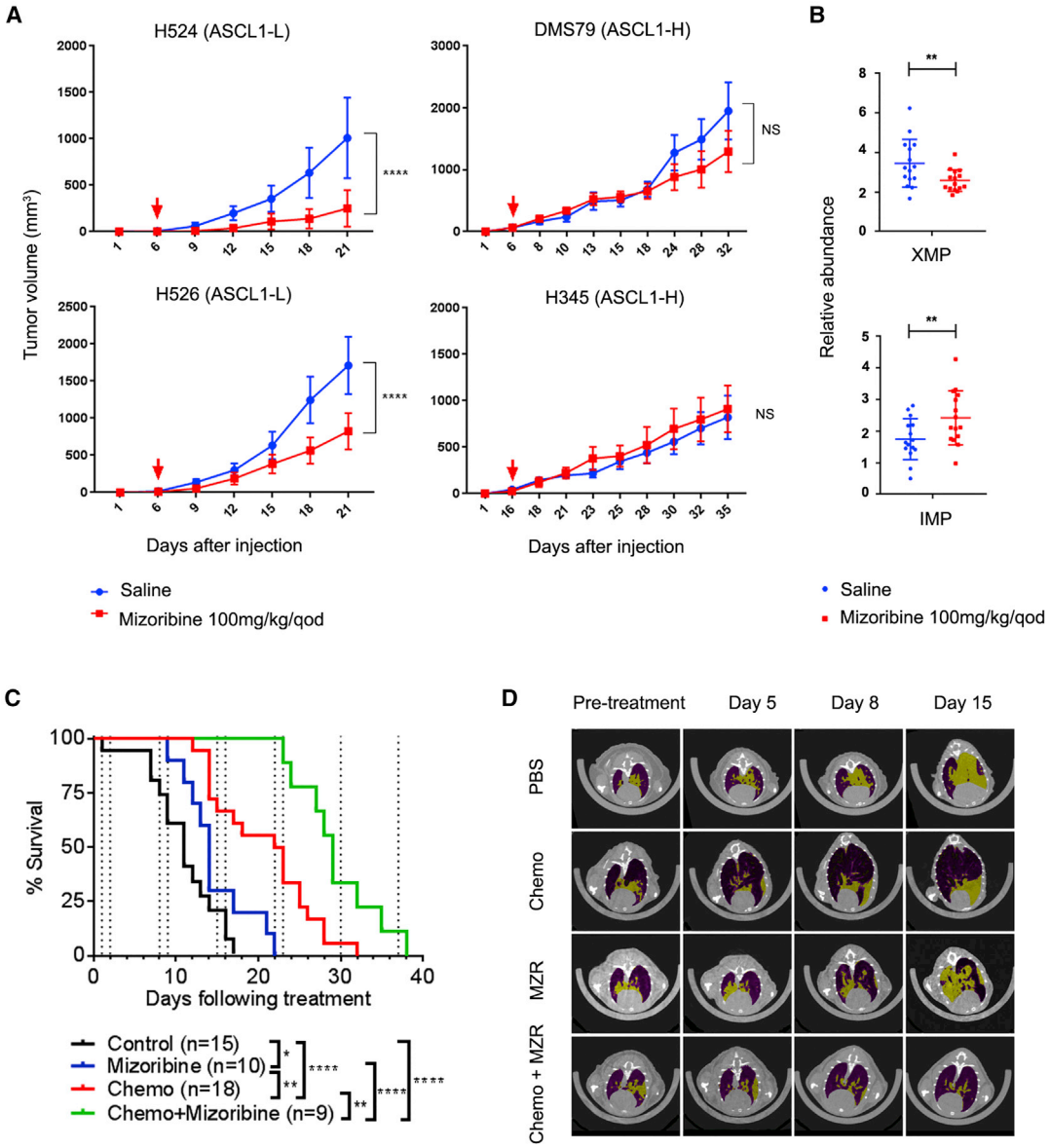

Figure 7. IMPDH Is a Druggable Target Required for ASCL1^{Low} SCLC Growth

(A) Growth of subcutaneous xenografts in NSG mice derived from two ASCL1^{High} and two ASCL1^{Low} cell lines treated with the IMPDH inhibitor mizoribine (100 mg/kg every other day). Mean tumor volume and SEM are shown for each group (n = 5 mice). The arrow indicates initiation of mizoribine dosing. ****p < 0.0001.

(B) Effect of mizoribine on XMP and IMP abundance in H524 xenografts. Individual data points are shown together with mean and SD for three independent tumor fragments from five mice in each group. **p < 0.01.

(C) Kaplan-Meier survival analysis of RPM mice treated with chemotherapy (cisplatin and etoposide) in combination with mizoribine. Cisplatin, 5 mg/kg once a week; etoposide, 10 mg/kg once a week; mizoribine, 100 mg/kg every other day. Dashed lines indicate chemotherapy treatment. From the fifth round of chemotherapy onward, mice were treated with etoposide, but not cisplatin. *p < 0.05; **p <0.01; ****p < 0.0001.

(D) Representative microCT images from RPM mice pseudo-colored to differentiate tumors (yellow) from normal tissues/airway (purple).

Transcriptional control of purine biosynthesis has also been reported for the mTORC1 signaling pathway, perhaps the most central regulator of anabolic metabolism in mammals (Ben-Sahra et al., 2016). Together these data place *de novo* purine nucleotide synthesis, particularly guanine nucleotide synthesis, as a key effector of multiple growth signals.

At least for the first several hours of IMPDH inhibition, the most impressive consequence of IMPDH inhibition in ASCL1^{Low} SCLC cells is the suppression of Pol I activity rather than the activity of Pol II, Pol III, or DNA synthesis. It is likely that sustained IMPDH inhibition and guanosine nucleotide depletion would more broadly perturb transcription and DNA synthesis. However, the acute effect on Pol I may be sufficient to explain the potent effect of IMPDH inhibitors on ASCL1^{Low} SCLC cell growth. Ribosome biogenesis is a major component of MYC-regulated anabolism (Grandori et al., 2005; Kim et al., 2000), and inhibition

of Pol I-mediated ribosomal DNA transcription extends survival of mice with MYC-driven B cell lymphoma (Dang, 2013; Devlin et al., 2016). Although the guanosine nucleotide guanosine triphosphate (GTP) has many functions in nucleic acid synthesis, signal transduction, and energy currency, its role in Pol I transcription is particularly relevant to ASCL1^{Low} SCLC with high levels of MYC. Recruitment of Pol I to the ribosomal DNA requires GTP binding to transcription initiation factor I (TIF-IA), and depleting GTP with MPA impairs Pol I's association with TIF-IA to suppress rRNA synthesis (Nguyen le et al., 2015). Overall, the importance of guanosine in ribosome biogenesis may explain why levels of purines, but not pyrimidines, distinguish ASCL1^{Low} from ASCL1^{High} SCLC lines.

Pharmacological inhibition of purine synthesis as a means to treat cancer has been investigated for many years, with IMPDH considered as a possible target (Christopherson et al., 2002; Hedstrom and Gan, 2006). Both MPA and mizoribine are already used in humans as immunosuppressants in organ transplantation and autoimmune diseases, with mizoribine in particular being well tolerated (Akiyama et al., 2005; Bergan et al., 2016; Kawasaki, 2009). However, evidence supporting the utility of IMPDH inhibitors in cancer is lacking, perhaps because dependence on IMPDH is determined at least in part by incompletely defined, cell-intrinsic factors (Lin et al., 2011). Our finding that ASCL1^{Low} SCLCs with high levels of MYC are sensitive to IMPDH inhibition *in vivo* suggests both enrollment biomarkers (NEUROD1 and high levels of MYC expression) and a new target for therapy in this intractable form of cancer.

Limitations of Study

We demonstrated a subtype-selective vulnerability defined by cell-autonomous factors, but how the tumor microenvironment modifies IMPDH dependence is still largely unknown. We have not yet defined metabolic phenotypes of primary human SCLC, and addressing this limitation is an important step in translating the findings. We have also not yet assessed mizoribine's efficacy in models of chemotherapeutic resistance. This is important because resistance to cytotoxic chemotherapy rapidly emerges in most human SCLCs. It will be interesting to test whether mizoribine retains its efficacy in tumors first subjected to cisplatin and/or etoposide.

STAR★METHODS

Detailed methods are provided in the online version of this paper and include the following:

SUPPLEMENTAL INFORMATION

Supplemental Information includes seven figures and one table and can be found with this article online at https://doi.org/10.1016/j.cmet.2018.06.005.

ACKNOWLEDGMENTS

We thank the DeBerardinis laboratory for critiquing the manuscript. We thank Brendan D. Manning for advice about GMP synthesis in cancer cells and mizoribine dosing in mice. We thank Luc Girard for help with the SCLC mRNA expression datasets, Jane E. Johnson for helping with data analysis of human SCLC samples, and Mary Calvaruso for pilot experiments in metabolic phenotyping of SCLC cell lines. R.J.D. is supported by grants from the NIH (1R35CA22044901), V Foundation (Translational Award), Robert A. Welch Foundation (I-1733), Howard Hughes Medical Institute (Faculty Scholars Program), Cancer Prevention and Research Institute of Texas (RP160089), Robert L. Moody, Sr. Faculty Scholar award, and Joel B. Steinberg Chair in Pediatrics. Z.H. is supported by Tsinghua University (grant no. 53332200517) and National Science and Technology Major Project for "Significant New Drug Development" (2017ZX09304015). F.H. is supported by Union Hospital, Tongji Medical College, Huazhong University of Science and Technology. J.D.M. and A.F.G. are supported by the University of Texas Specialized Programs of Research Excellence (SPORE) (P50CA70907) and SCLC U24 CA213274 grants. T.G.O. was supported in part by ACS Research Scholar Award RSG-13-300-01-TBG, NIH award R01CA187457, and the Damon Runyon Cancer Research Foundation DRR-26-13.

AUTHOR CONTRIBUTIONS

F.H., Z.H., and R.J.D. conceived the project, designed the experiments, interpreted the data, and wrote the manuscript. W.G. assisted in writing the manuscript. F.H. performed experiments related to SCLC cell lines and xenografts. K.E.H., A.F.G., and J.D.M. provided SCLC cell lines and expertise in biological and clinical aspects of human SCLC. T.G.O. provided mouse models of SCLC and helped design and interpret experiments involving these mice. J.K., X.S., M.N., M.D.C., A.S.I., and L.C. assisted in data acquisition, analysis, and interpretation. K.L., A.K.K., and X.L. provided molecular biology reagents and expertise in cell biology. Z.H. developed the metabolomics approach, supervised metabolomic analyses, and aided in data interpretation. Z.H. and F.C. developed methods for isotope labeling in purines. L.G.Z. and F.C. performed metabolomics and isotope tracing experiments.

DECLARATION OF INTERESTS

R.J.D. is an advisor for Agios Pharmaceuticals.

Received: October 12, 2017
Revised: April 16, 2018
Accepted: June 4, 2018
Published: June 28, 2018

REFERENCES

Akiyama, T., Okazaki, H., Takahashi, K., Hasegawa, A., Tanabe, K., Uchida, K., Takahara, S., and Toma, H. (2005). Mizoribine in combination therapy with tacrolimus for living donor renal transplantation: analysis of a nationwide study in Japan. Transplant Proc. *37*, 843–845.

Antonia, S.J., Lopez-Martin, J.A., Bendell, J., Ott, P.A., Taylor, M., Eder, J.P., Jager, D., Pietanza, M.C., Le, D.T., de Braud, F., et al. (2016). Nivolumab alone and nivolumab plus ipilimumab in recurrent small-cell lung cancer (CheckMate 032): a multicentre, open-label, phase 1/2 trial. Lancet Oncol. *17*, 883–895.

Augustyn, A., Borromeo, M., Wang, T., Fujimoto, J., Shao, C., Dospoy, P.D., Lee, V., Tan, C., Sullivan, J.P., Larsen, J.E., et al. (2014). ASCL1 is a lineage oncogene providing therapeutic targets for high-grade neuroendocrine lung cancers. Proc. Natl. Acad. Sci. USA *111*, 14788–14793.

Barretina, J., Caponigro, G., Stransky, N., Venkatesan, K., Margolin, A.A., Kim, S., Wilson, C.J., Lehar, J., Kryukov, G.V., Sonkin, D., et al. (2012). The cancer cell line encyclopedia enables predictive modelling of anticancer drug sensitivity. Nature *483*, 603–607.

Ben-Sahra, I., Hoxhaj, G., Ricoult, S.J., Asara, J.M., and Manning, B.D. (2016). mTORC1 induces purine synthesis through control of the mitochondrial tetrahydrofolate cycle. Science *351*, 728–733.

Bergan, S., Bremer, S., and Vethe, N.T. (2016). Drug target molecules to guide immunosuppression. Clin. Biochem. *49*, 411–418.

Boroughs, L.K., and DeBerardinis, R.J. (2015). Metabolic pathways promoting cancer cell survival and growth. Nat. Cell. Biol. *17*, 351–359.

Borromeo, M.D., Savage, T.K., Kollipara, R.K., He, M., Augustyn, A., Osborne, J.K., Girard, L., Minna, J.D., Gazdar, A.F., Cobb, M.H., et al. (2016). ASCL1 and NEUROD1 reveal heterogeneity in pulmonary neuroendocrine tumors and regulate distinct genetic programs. Cell Rep. *16*, 1259–1272.

Buescher, J.M., Antoniewicz, M.R., Boros, L.G., Burgess, S.C., Brunengraber, H., Clish, C.B., DeBerardinis, R.J., Feron, O., Frezza, C., Ghesquiere, B., et al. (2015). A roadmap for interpreting (13)C metabolite labeling patterns from cells. Curr. Opin. Biotechnol. *34*, 189–201.

Byers, L.A., Diao, L., Wang, J., Saintigny, P., Girard, L., Peyton, M., Shen, L., Fan, Y., Giri, U., Tumula, P.K., et al. (2013). An epithelial-mesenchymal transition gene signature predicts resistance to EGFR and PI3K inhibitors and identifies Axl as a therapeutic target for overcoming EGFR inhibitor resistance. Clin. Cancer Res. *19*, 279–290.

Christopherson, R.I., Lyons, S.D., and Wilson, P.K. (2002). Inhibitors of de novo nucleotide biosynthesis as drugs. Acc. Chem. Res. *35*, 961–971.

Dang, C.V. (2013). MYC, metabolism, cell growth, and tumorigenesis. Cold Spring Harb. Perspect. Med. *3*, https://doi.org/10.1101/cshperspect.a014217.

Demedts, I.K., Vermaelen, K.Y., and van Meerbeeck, J.P. (2010). Treatment of extensive-stage small cell lung carcinoma: current status and future prospects. Eur. Respir. J. *35*, 202–215.

Devlin, J.R., Hannan, K.M., Hein, N., Cullinane, C., Kusnadi, E., Ng, P.Y., George, A.J., Shortt, J., Bywater, M.J., Poortinga, G., et al. (2016). Combination therapy targeting ribosome biogenesis and mRNA translation synergistically extends survival in MYC-driven lymphoma. Cancer Discov. *6*, 59–70.

Gazdar, A.F., Carney, D.N., Nau, M.M., and Minna, J.D. (1985). Characterization of variant subclasses of cell lines derived from small cell lung cancer having distinctive biochemical, morphological, and growth properties. Cancer Res. *45*, 2924–2930.

Gazdar, A.F., Savage, T.K., Johnson, J.E., Berns, A., Sage, J., Linnoila, R.I., MacPherson, D., McFadden, D.G., Farago, A., Jacks, T., et al. (2015). The comparative pathology of genetically engineered mouse models for neuroendocrine carcinomas of the lung. J. Thorac. Oncol. *10*, 553–564.

George, J., Lim, J.S., Jang, S.J., Cun, Y., Ozretic, L., Kong, G., Leenders, F., Lu, X., Fernandez-Cuesta, L., Bosco, G., et al. (2015). Comprehensive genomic profiles of small cell lung cancer. Nature *524*, 47–53.

Govindan, R., Page, N., Morgensztern, D., Read, W., Tierney, R., Vlahiotis, A., Spitznagel, E.L., and Piccirillo, J. (2006). Changing epidemiology of small-cell lung cancer in the United States over the last 30 years: analysis of the surveillance, epidemiologic, and end results database. J. Clin. Oncol. *24*, 4539–4544.

Grandori, C., Gomez-Roman, N., Felton-Edkins, Z.A., Ngouenet, C., Galloway, D.A., Eisenman, R.N., and White, R.J. (2005). c-Myc binds to human ribosomal DNA and stimulates transcription of rRNA genes by RNA polymerase I. Nat. Cell. Biol. *7*, 311–318.

Hedstrom, L., and Gan, L. (2006). IMP dehydrogenase: structural schizophrenia and an unusual base. Curr. Opin. Chem. Biol. *10*, 520–525.

Hensley, C.T., Faubert, B., Yuan, Q., Lev-Cohain, N., Jin, E., Kim, J., Jiang, L., Ko, B., Skelton, R., Loudat, L., et al. (2016). Metabolic heterogeneity in human lung tumors. Cell *164*, 681–694.

Hu, J., Locasale, J.W., Bielas, J.H., O'Sullivan, J., Sheahan, K., Cantley, L.C., Vander Heiden, M.G., and Vitkup, D. (2013). Heterogeneity of tumor-induced gene expression changes in the human metabolic network. Nat. Biotechnol. *31*, 522–529.

Ishikawa, H. (1999). Mizoribine and mycophenolate mofetil. Curr. Med. Chem. *6*, 575–597.

Johnson, B.E., Brennan, J.F., Ihde, D.C., and Gazdar, A.F. (1992). myc family DNA amplification in tumors and tumor cell lines from patients with small-cell lung cancer. J. Natl. Cancer Inst. Monogr. 39–43.

Kawasaki, Y. (2009). Mizoribine: a new approach in the treatment of renal disease. Clin. Dev. Immunol. *2009*, 681482.

Kim, H.S., Mendiratta, S., Kim, J., Pecot, C.V., Larsen, J.E., Zubovych, I., Seo, B.Y., Kim, J., Eskiocak, B., Chung, H., et al. (2013). Systematic identification of molecular subtype-selective vulnerabilities in non-small-cell lung cancer. Cell *155*, 552–566.

Kim, J., Hu, Z., Cai, L., Li, K., Choi, E., Faubert, B., Bezwada, D., Rodriguez-Canales, J., Villalobos, P., Lin, Y.F., et al. (2017). CPS1 maintains pyrimidine pools and DNA synthesis in KRAS/LKB1-mutant lung cancer cells. Nature *546*, 168–172.

Kim, S., Li, Q., Dang, C.V., and Lee, L.A. (2000). Induction of ribosomal genes and hepatocyte hypertrophy by adenovirus-mediated expression of c-Myc in vivo. Proc. Natl. Acad. Sci. USA *97*, 11198–11202.

Koehl, G.E., Wagner, F., Stoeltzing, O., Lang, S.A., Steinbauer, M., Schlitt, H.J., and Geissler, E.K. (2007). Mycophenolate mofetil inhibits tumor growth and angiogenesis in vitro but has variable antitumor effects in vivo, possibly related to bioavailability. Transplantation *83*, 607–614.

Koh, C.M., Gurel, B., Sutcliffe, S., Aryee, M.J., Schultz, D., Iwata, T., Uemura, M., Zeller, K.I., Anele, U., Zheng, Q., et al. (2011). Alterations in nucleolar structure and gene expression programs in prostatic neoplasia are driven by the MYC oncogene. Am. J. Pathol. *178*, 1824–1834.

Li, B., Qiu, B., Lee, D.S., Walton, Z.E., Ochocki, J.D., Mathew, L.K., Mancuso, A., Gade, T.P., Keith, B., Nissim, I., et al. (2014). Fructose-1,6-bisphosphatase opposes renal carcinoma progression. Nature *513*, 251–255.

Lin, C.Y., Loven, J., Rahl, P.B., Paranal, R.M., Burge, C.B., Bradner, J.E., Lee, T.I., and Young, R.A. (2012). Transcriptional amplification in tumor cells with elevated c-Myc. Cell *151*, 56–67.

Lin, T., Meng, L., and Tsai, R.Y. (2011). GTP depletion synergizes the anti-proliferative activity of chemotherapeutic agents in a cell type-dependent manner. Biochem. Biophys. Res. Commun. *414*, 403–408.

Liu, Y., Marks, K., Cowley, G.S., Carretero, J., Liu, Q., Nieland, T.J., Xu, C., Cohoon, T.J., Gao, P., Zhang, Y., et al. (2013). Metabolic and functional genomic studies identify deoxythymidylate kinase as a target in LKB1-mutant lung cancer. Cancer Discov. *3*, 870–879.

Liu, Y.C., Li, F., Handler, J., Huang, C.R., Xiang, Y., Neretti, N., Sedivy, J.M., Zeller, K.I., and Dang, C.V. (2008). Global regulation of nucleotide biosynthetic genes by c-Myc. PLoS One *3*, e2722.

Mannava, S., Grachtchouk, V., Wheeler, L.J., Im, M., Zhuang, D., Slavina, E.G., Mathews, C.K., Shewach, D.S., and Nikiforov, M.A. (2008). Direct role of nucleotide metabolism in C-MYC-dependent proliferation of melanoma cells. Cell Cycle *7*, 2392–2400.

McFadden, D.G., Papagiannakopoulos, T., Taylor-Weiner, A., Stewart, C., Carter, S.L., Cibulskis, K., Bhutkar, A., McKenna, A., Dooley, A., Vernon, A., et al. (2014). Genetic and clonal dissection of murine small cell lung carcinoma progression by genome sequencing. Cell *156*, 1298–1311.

Minna, J.D., Rudin, C., and the Small Cell Lung Cancer Working Group of the National Cancer Institute's Clinical Trials and Translational Research Advisory Committee (CTAC). (2014). Scientific Framework for Small Cell Lung Cancer. https://deainfo.nci.nih.gov/advisory/ctac/workgroup/SCLC/SCLC%20Congressional%20Response.pdf.

Mollaoglu, G., Guthrie, M.R., Bohm, S., Bragelmann, J., Can, I., Ballieu, P.M., Marx, A., George, J., Heinen, C., Chalishazar, M.D., et al. (2017). MYC drives

progression of small cell lung cancer to a variant neuroendocrine subtype with vulnerability to aurora kinase inhibition. Cancer Cell *31*, 270–285.

Nguyen le, X.T., Lee, Y., Urbani, L., Utz, P.J., Hamburger, A.W., Sunwoo, J.B., and Mitchell, B.S. (2015). Regulation of ribosomal RNA synthesis in T cells: requirement for GTP and Ebp1. Blood *125*, 2519–2529.

Peifer, M., Fernandez-Cuesta, L., Sos, M.L., George, J., Seidel, D., Kasper, L.H., Plenker, D., Leenders, F., Sun, R., Zander, T., et al. (2012). Integrative genome analyses identify key somatic driver mutations of small-cell lung cancer. Nat. Genet. *44*, 1104–1110.

Poirier, J.T., Dobromilskaya, I., Moriarty, W.F., Peacock, C.D., Hann, C.L., and Rudin, C.M. (2013). Selective tropism of Seneca Valley virus for variant subtype small cell lung cancer. J. Natl. Cancer Inst. *105*, 1059–1065.

Poirier, J.T., Gardner, E.E., Connis, N., Moreira, A.L., de Stanchina, E., Hann, C.L., and Rudin, C.M. (2015). DNA methylation in small cell lung cancer defines distinct disease subtypes and correlates with high expression of EZH2. Oncogene *34*, 5869–5878.

Pozzo, F., Bittolo, T., Vendramini, E., Bomben, R., Bulian, P., Rossi, F.M., Zucchetto, A., Tissino, E., Degan, M., D'Arena, G., et al. (2017). NOTCH1-mutated chronic lymphocytic leukemia cells are characterized by a MYC-related overexpression of nucleophosmin 1 and ribosome-associated components. Leukemia *31*, 2407–2415.

Rekhtman, N. (2010). Neuroendocrine tumors of the lung: an update. Arch. Pathol. Lab. Med. *134*, 1628–1638.

Rudin, C.M., Durinck, S., Stawiski, E.W., Poirier, J.T., Modrusan, Z., Shames, D.S., Bergbower, E.A., Guan, Y., Shin, J., Guillory, J., et al. (2012). Comprehensive genomic analysis identifies SOX2 as a frequently amplified gene in small-cell lung cancer. Nat. Genet. *44*, 1111–1116.

Sabo, A., Kress, T.R., Pelizzola, M., de Pretis, S., Gorski, M.M., Tesi, A., Morelli, M.J., Bora, P., Doni, M., Verrecchia, A., et al. (2014). Selective transcriptional regulation by Myc in cellular growth control and lymphomagenesis. Nature *511*, 488–492.

Schaffer, B.E., Park, K.S., Yiu, G., Conklin, J.F., Lin, C., Burkhart, D.L., Karnezis, A.N., Sweet-Cordero, E.A., and Sage, J. (2010). Loss of p130 accelerates tumor development in a mouse model for human small-cell lung carcinoma. Cancer Res. *70*, 3877–3883.

Stine, Z.E., Walton, Z.E., Altman, B.J., Hsieh, A.L., and Dang, C.V. (2015). MYC, metabolism, and cancer. Cancer Discov. *5*, 1024–1039.

Sutherland, K.D., Proost, N., Brouns, I., Adriaensen, D., Song, J.Y., and Berns, A. (2011). Cell of origin of small cell lung cancer: inactivation of Trp53 and Rb1 in distinct cell types of adult mouse lung. Cancer Cell *19*, 754–764.

Travis, W.D. (2010). Advances in neuroendocrine lung tumors. Ann. Oncol. *21* (*Suppl 7*), vii65–71.

Valvezan, A.J., Turner, M., Belaid, A., Lam, H.C., Miller, S.K., McNamara, M.C., Baglini, C., Housden, B.E., Perrimon, N., Kwiatkowski, D.J., et al. (2017). mTORC1 couples nucleotide synthesis to nucleotide demand resulting in a targetable metabolic vulnerability. Cancer Cell *32*, 624–638.e5.

Vander Heiden, M.G., and DeBerardinis, R.J. (2017). Understanding the intersections between metabolism and cancer biology. Cell *168*, 657–669.

Xia, J., and Wishart, D.S. (2016). Using metaboanalyst 3.0 for comprehensive metabolomics data analysis. Curr. Protoc. Bioinformatics *55*, 14.10.1–14.10.91.

Yu, J.B., Decker, R.H., Detterbeck, F.C., and Wilson, L.D. (2010). Surveillance epidemiology and end results evaluation of the role of surgery for stage I small cell lung cancer. J. Thorac. Oncol. *5*, 215–219.

STAR★METHODS

KEY RESOURCES TABLE

REAGENT or RESOURCE	SOURCE	IDENTIFIER
Antibodies		
ASCL1	BD Bioscience	Cat# 556604; **RRID:AB_396479**
ACTB	Sigma	Cat# A3854; **RRID:AB_262011**
IMPDH1	Sigma	Cat# SAB2101156; **RRID:AB_10605164**
IMPDH2	Abcam	Cat# ab131158; **RRID:AB_11156264**
MYC	Cell Signaling	Cat# 9402; **RRID:AB_2151827**
MYC	Cell Signaling	Cat# 13987; **RRID:AB_2631168**
GMPS	Cell Signaling	Cat# 14602
MAT2A	Abcam	Cat# ab77471; **RRID:AB_1566406**
H3K27Ac	Active Motif	Cat# 39133; **RRID:AB_2561016**
NEUROD1	Santa Cruz	Cat# sc-1084; **RRID:AB_630922**
Cleaved Caspase-3	Cell Signaling	Cat# 9664; **RRID:AB_2070042**
mTOR	Cell Signaling	Cat# 9862; **RRID:AB_10696885**
Phospho-mTOR S2448	Cell Signaling	Cat# 9862; **RRID:AB_10696885**
Phospho-4EBP1 T37/46	Cell Signaling	Cat# 9862; **RRID:AB_10696885**
Phospho-p70 S6 Kinase T389	Cell Signaling	Cat# 9234; **RRID:AB_2269803**
Phospho-S6 S235/236	Cell Signaling	Cat# 4858; **RRID:AB_916156**
Chemicals, Peptides, and Recombinant Proteins		
L-Glutamine (amide-^{15}N)	Cambridge Isotope Laboratories	Cat# NLM-557-1
D-Glucose (U-^{13}C6)	Cambridge Isotope Laboratories	Cat# CLM-1396-5
Mycophenolic acid	Selleck Chemicals	Cat# S2487
Cycloleucine	Sigma	Cat# A48105
Guanosine	Sigma	Cat# G6752
Mizoribine	Sigma	Cat# M3047
Cisplatin	Sigma	Cat# PHR1624
Etoposide	Sigma	Cat# E1383
Trypan blue	Sigma	Cat# T8154
Propidium iodide	Sigma	Cat# P4170
Torin 1	Selleck Chemicals	Cat# S2827
Pemetrexed	Thermo Fisher	Cat# 50-672-8
DMSO	Sigma	Cat# D2650
Protease inhibitor cocktail	Roche	Cat# 11873580001
Phosphatase Inhibitor	Roche	Cat# 04906845001
Puromycin	Sigma	Cat# P8833
Accutase	Thermo Fisher	Cat# A1110501
Critical Commercial Assays		
Cell Titer Glo luminescent cell viability assay	Promega	Cat# G7573
Annexin V-FITC staining kit	Thermo Fisher	Cat# BDB556420
Senescence β-Galactosidase staining kit	Cell Signaling	Cat# 9860
Experimental Models: Cell Lines		
NCIH2107	Hamon Cancer Center	Augustyn et al., 2014
NCIH1672	Hamon Cancer Center	Augustyn et al., 2014
NCIH128	Hamon Cancer Center	Augustyn et al., 2014
NCIH865	Hamon Cancer Center	Augustyn et al., 2014

(*Continued on next page*)

Continued

REAGENT or RESOURCE	SOURCE	IDENTIFIER
NCIH146	Hamon Cancer Center	Augustyn et al., 2014
NCIH889	Hamon Cancer Center	Augustyn et al., 2014
NCIH187	Hamon Cancer Center	Augustyn et al., 2014
NCIH345	Hamon Cancer Center	Augustyn et al., 2014
NCIH748	Hamon Cancer Center	Augustyn et al., 2014
NCIH1514	Hamon Cancer Center	Augustyn et al., 2014
NCIH69	Hamon Cancer Center	Augustyn et al., 2014
NCIH1184	Hamon Cancer Center	Augustyn et al., 2014
NCIH2141	Hamon Cancer Center	Augustyn et al., 2014
NCIH209	Hamon Cancer Center	Augustyn et al., 2014
NCIH289	Hamon Cancer Center	Augustyn et al., 2014
NCIH510	Hamon Cancer Center	Augustyn et al., 2014
NCIH1238	Hamon Cancer Center	Augustyn et al., 2014
NCIH2195	Hamon Cancer Center	Augustyn et al., 2014
NCIH82	Hamon Cancer Center	Augustyn et al., 2014
NCIH211	Hamon Cancer Center	Augustyn et al., 2014
NCIH526	Hamon Cancer Center	Augustyn et al., 2014
HCC970	Hamon Cancer Center	Augustyn et al., 2014
NCIH524	Hamon Cancer Center	Augustyn et al., 2014
NCIH2171	Hamon Cancer Center	Augustyn et al., 2014
NCIH2227	Hamon Cancer Center	Augustyn et al., 2014
NCIH378	Hamon Cancer Center	Augustyn et al., 2014
HCC33	Hamon Cancer Center	Augustyn et al., 2014
NCIH1607	Hamon Cancer Center	Augustyn et al., 2014
NCIH1628	Hamon Cancer Center	Augustyn et al., 2014
NCIH2029	Hamon Cancer Center	Augustyn et al., 2014
NCIH3282	Hamon Cancer Center	Augustyn et al., 2014
NCIH1522	Hamon Cancer Center	Augustyn et al., 2014
NCIH1836	Hamon Cancer Center	Augustyn et al., 2014
NCIH60	Hamon Cancer Center	Augustyn et al., 2014
NCIH1048	Hamon Cancer Center	Augustyn et al., 2014
NCIH1092	Hamon Cancer Center	Augustyn et al., 2014
NCIH1284	Hamon Cancer Center	Augustyn et al., 2014
SHP77	Hamon Cancer Center	Augustyn et al., 2014
HCC4000	Hamon Cancer Center	Augustyn et al., 2014
HCC1772	Hamon Cancer Center	Augustyn et al., 2014
HCC4001	Hamon Cancer Center	Augustyn et al., 2014
HCC4002	Hamon Cancer Center	Augustyn et al., 2014
HCC4004	Hamon Cancer Center	Augustyn et al., 2014
HCC4005	Hamon Cancer Center	Augustyn et al., 2014
NCIH1694	Hamon Cancer Center	Augustyn et al., 2014
NCIH1770	Hamon Cancer Center	Augustyn et al., 2014
NCIH2769	Hamon Cancer Center	Augustyn et al., 2014
NCIH446	Hamon Cancer Center	Augustyn et al., 2014
Experimental Models: Organisms/Strains		
Mouse: NOD.Cg-Prkdc^{scid} Il2rg^{tm1Wjl}/SzJArc	UT Southwestern	**RRID:IMSR_ARC:NSG**
Mouse: STOCK Igs2$^{tm1(CAG-Myc*T58A/luc)Wrey}$Trp53^{tm1Brn}Rb1^{tm3Tyj}/OlvrJ	Provided by Trudy G. Oliver	Mollaoglu et al., 2017

(*Continued on next page*)

Continued

REAGENT or RESOURCE	SOURCE	IDENTIFIER
Oligonucleotides		
gRNAs for CRISPR/Cas9-mediated knockout, see Table S1	IDT DNA	N/A
Primers for qPCR, see Table S1	IDT DNA	N/A
Primers for MYC overexpression, see Table S1	IDT DNA	N/A
Software and Algorithms		
MultiQuant version 2.1	Applied Biosystems SCIEX	N/A
SIMCA-P	Umetrics	N/A
Metaboanalyst 3.0	Xia and Wishart, 2016	http://www.metaboanalyst.ca/
Other		
e-Myco mycoplasma PCR detection kit	Bulldog Bio	Cat# 2523348
Matrigel	BD Biosciences	Cat# 356237
RPMI-1640	Sigma	Cat# R8758
Fetal bovine serum	Gemini Bio-Products	Cat# 100-106
Dialyzed fetal bovine serum	Gemini Bio-Products	Cat# 100-108
TRIzol	Thermo Fisher	Cat# 15596018
iScript cDNA synthesis kit	BioRad	Cat# 1708891
SYBR Green PCR system	Invitrogen	Cat# 4364344
ECL Western Blotting Substrate	Thermo Fisher	Cat# 32106
lentiCRISPR v2	Addgene	Cat# 52961
MGC Human MYC Sequence-Verified cDNA	Dharmacon	Cat# MHS6278-202755482
pLVX-TRE3G-IRES expression system	Clonetech	Cat# 631362
pGL4.11[luc2P]	Promega	Cat# E6651
FuGENE 6 transfection reagent	Promega	Cat# E2691
Dual-Luciferase reporter assay system	Promega	Cat# E1910

CONTACT FOR REAGENT AND RESOURCE SHARING

Further information and requests for resources and reagents should be directed to and will be fulfilled by the Lead Contact, Ralph J. DeBerardinis (ralph.deberardinis@utsouthwestern.edu).

EXPERIMENTAL MODEL AND SUBJECT DETAILS

Cell Lines

All cell lines were obtained from the Hamon Cancer Center Collection (University of Texas Southwestern Medical Center). Cells were cultured as small spheres in RPMI 1640 medium (Sigma #R8758) supplemented with 10% fetal bovine serum (Gemini Bio-Products #100-106) and penicillin/streptomycin, at 37°C in a humidified atmosphere containing 5% CO_2. All cell lines were DNA-fingerprinted as described by PowerPlex system (Augustyn et al., 2014) and verified as mycoplasma free with e-Myco kit (Bulldog Bio #2523348).

Mouse Studies

Xenograft procedures were performed with the approval of the University of Texas Southwestern Medical Center IACUC. SCLC cells were suspended in a 1:1 mixture of Matrigel (BD Bioscience #356237) and RPMI 1640 mixture, then 0.5-2 x 10^6 cells were implanted subcutaneously into 6-8-week-old NSG mice (Jackson Laboratory #005557). Mice were randomized after tumor cell injection. 100mg/kg mizoribine (Sigma #M3047) in saline or saline was injected intraperitoneally every other day when tumors were palpable. Tumor size was measured using calipers and calculated by short (a) and long (b) diameters (volume=$a^2b/2$).

RPM mouse generation, microCT imaging and survival studies were performed as described previously (Mollaoglu et al., 2017). RPP mice were kindly provided by David MacPherson. RPM and RPP mice were housed in an environmentally controlled room and all experiments were performed in accordance with University of Utah's Institutional Animal Care and Use Committee. When tumor burden reached 10-12% of the total pulmonary volume by microCT imaging, chemotherapy was initiated. Once a week, mice were given freshly prepared cisplatin (Sigma, PHR1624) in PBS on Day 1 and etoposide (Sigma, E1383) in 70% PEG in water on Day 2. Both drugs were administered by intraperitoneal injection. From the 5th week onwards, mice were given etoposide but not cisplatin. Freshly prepared mizoribine (Sigma #M3047) in saline was given at 100 mg/kg every other day by intraperitoneal injection from Day 1 of therapy until the end of the experiment.

METHOD DETAILS

Metabolomics

Cells were incubated in fresh RPMI 1640 media for 2 hours, washed with ice-cold saline, quenched with 80% methanol and subjected to three rapid freeze-thaw cycles. The debris was pelleted by centrifugation at 4°C and the supernatant containing aqueous metabolites was collected and evaporated to dryness using a SpeedVac concentrator. Metabolites were reconstituted in 100 μl of 0.03% formic acid in analytical-grade water, vortexed and centrifuged to remove insoluble material. The supernatant was collected and subjected to targeted metabolomics analysis as described on an AB SCIEX QTRAP 5500 liquid chromatography/triple quadrupole mass spectrometer (Applied Biosystems SCIEX) (Kim et al., 2017). The injection volume was 20 μl. Chromatogram review and peak area integration were performed using MultiQuant (version 2.1, Applied Biosystems SCIEX). The peak area for each detected metabolite was normalized against the total ion count of that sample.

Normalized peak areas were used as variables for multivariate and univariate statistical data analyses. Preprocessed data sets were mean-centered and unit-variance scaled, then evaluated by principal component analysis to visualize clustering and detect outliers using SIMCA-P (version 13.0.1, Umetrics). Hierarchical clustering and partial least squares discriminant analysis and variable importance in projection analysis were done using Metaboanalyst 3.0 (Xia and Wishart, 2016).

^{15}N-glutamine and ^{13}C-glucose Labeling

Cells were incubated in RPMI 1640 media supplemented with dialyzed fetal bovine serum (Gemini Bio-Products #100-108) containing 0.3 mg/ml [amide-^{15}N]glutamine or 2 mg/ml [U-^{13}C]glucose for the indicated duration, washed with ice-cold saline, quenched with 80% methanol and subjected to three freeze-thaw cycles. The debris was pelleted by centrifugation at 4°C and the supernatant was collected and evaporated to dryness using a SpeedVac concentrator. Metabolites were reconstituted in 50 μl of 0.03% formic acid in analytical-grade water, vortexed and centrifuged to remove insoluble material. The supernatant was collected and analyzed as described previously with modifications using an AB QTRAP 5500 liquid chromatography/triple quadrupole mass spectrometer (Applied Biosystems SCIEX) (Kim et al., 2017). The modifications were as follows. Gradient program: 0-1 min, 1% B; 1-4 min, 1-100% B; 4-7.5 min, 100% B; 7.5-7.6 min, 100-1% B; 7.6-10 min, 1% B. Injection volume: 5 μl. Dwelling time for each transition: 20 ms. MRM data were acquired using Analyst software (version 1.6.1, Applied Biosystems SCIEX).

qRT-PCR

Total RNA from cells was extracted and isolated with TRIzol (Thermo Fisher #15596018). cDNA was generated with the iScript cDNA synthesis kit (BioRad #1708891). Relative cDNA abundance was measured with the CYBR Green PCR system (Invitrogen #4364344) and data were normalized by beta-actin. Primers used for qPCR reactions were shown in Key Resources Table.

Western Blot

Protein lysates from SCLC lines and murine tumors were prepared in RIPA buffer, supplemented with PhosSTOP phosphatase and cOmplete protease inhibitor cocktail (Roche #11873580001, #04906845001). Protein samples were quantified with the BCA assay. Samples were separated on 4-20% SDS-PAGE gels, transferred to PVDF membranes, and probed with antibodies against ASCL1 (BD Bioscience #556604); ACTB (Sigma #A3854); IMPDH1 (Sigma #SAB2101156); IMPDH2 (Abcam #ab131158); MAT2A (Abcam #ab77471); MYC (Cell Signaling #5605); GMPS (Cell Signaling #14602); Cleaved Caspase-3 (Cell Signaling #9664); mTOR (Cell Signaling #9862); Phospho-mTOR S2448 (Cell Signaling #9862); Phospho-4EBP1 T37/46 (Cell Signaling #9862); Phospho-p70 S6 Kinase T389 (Cell Signaling #9234); Phospho-S6 S235/236 (Cell Signaling #4858). Bands were detected with the ECL blotting system (Pierce #32106).

CRISPR/Cas9-Mediated Editing and MYC Overexpression

IMPDH1, *IMPDH2*, *MAT2A* and *MYC* knockout cells were generated using the lentiCRISPRv2 system (Addgene #52961). SCLC cells grow in spheroids rather than single clones, so pools of cells infected with the empty vector or vectors with gene-targeting guide RNAs (gRNAs) were selected in puromycin (Sigma #P8833). gRNAs used to generate functional knockouts are in the Key Resources Table. For ectopic expression of MYC, the protein coding region of *MYC* (Dharmacon #MHS6278-202755482) was cloned and introduced into cells following the protocol by pLVX-TRE3G-IRES doxycycline inducible overexpression system (Clonetech #631362).

ChIP-Seq

Individual lung tumors from RPM mice were collected upon dissection, flash frozen and stored at -80°C until chromatin immunoprecipitation (ChIP). Tumors were prepared for ChIP by pulverizing frozen tissue into a fine powder. Samples were resuspended in 10 ml PBS and DNA was crosslinked in 1% formaldehyde. Fixation was terminated by adding glycine to a final concentration of 0.125 M. Chromatin was sheared using a Diagenode Bioruptor for 6 min on high power with 30 sec on-off cycles. 100 μg mouse tumor chromatin was immunoprecipitated with 5 μg rabbit anti-MYC (Cell Signaling #13987), 5 μg rabbit anti-H3K27Ac (Active-Motif #39133), 5 μg mouse anti-ASCL1 antibody (BD Biosciences #556604), 5 μg goat anti-NEUROD1 (Santa Cruz #sc-1084) followed by either anti-rabbit Dynabeads, anti-mouse DynaBeads or Protein G Dynabeads. The immunoprecipitated chromatin was purified with the Zymo ChIP DNA Clean and Concentrator kit. Mouse ChIP-Seq libraries were prepared using the NEBNext ChIP-Seq Library kit. Libraries were sequenced on an Illumina HiSeq 2500 as single-end 50 bp reads to a minimum depth of 35 million reads per sample. Reads were

aligned to the mm10 build of the mouse genome with bowtie using the following parameters: -m 1 -t –best -q -S -l 32 -e 80 -n 2. Peaks were called with MACS2 using a p value cutoff of $1e^{10}$ and the mfold parameter bounded between 15 and 100. For visualization, MACS2 produced bedgraphs with the –B and –SPMR options.

Cell Growth, Viability, Death and Senescence Assays

To evaluate cell proliferation in culture, 1-5 x 10^5 cells were seeded in 6-well plates and cultured as spheroids for 3 days, then digested with Accutase (Stem Cell Technologies #A1110501) into single cell suspensions and counted with a hemocytometer. To examine cell viability after drug treatment or genetic manipulation, cells were seeded in 24-well plates as spheroids and cultured for 3 days, then live cell content was measured with the CellTiter-Glo luminescent cell viability kit (Promega #7573). After treatment with the indicated drugs, cell death and senescence were evaluated following manufacturer-supplied protocols for the Annexin V-FITC/Propidium iodide kit (Thermo Fisher #BDB556420) and the Senescence β-Galactosidase staining kit (Cell Signaling #9860).

Soft-Agar Colony-Formation Assay

2-3 x 10^4 cells were suspended in 0.375% agar pre-equilibrated with RPMI 1640 supplemented with 10% fetal bovine serum, over a 0.75% bottom agar layer in a 6-well plate. Colonies were monitored for two weeks with intermittent medium supplementation with or without MPA. Images were acquired with G box-Syngene and colonies were detected with GeneTools software.

Promoter Luciferase Assay

The genomic regions containing wild-type or mutant alleles of the *IMPDH2* promoter were cloned into the firefly luciferase reporter construct pGL4.11[luc2P] (Promega #E6651). One μg of each reporter construct was cotransfected with 50 ng pRL-SV40-Renilla luciferase into H82 cells using FuGENE 6 transfection reagent (Promega #E2691). Cells were harvested after 48 hours and luciferase activity was measured using the Dual-Luciferase Assay system (Promega #1910) according to the manufacturer's protocol.

QUANTIFICATION AND STATISTICAL ANALYSIS

No methods were used to predetermine sample size. Metabolomics of cells and tumors were performed once with multiple replicates. Mizoribine and chemotherapy treatment of RPM mice was performed once. Data in the remaining figure panels reflect 2-3 independent experiments. Samples for metabolomics and isotope tracing were randomized before LC–MS/MS analysis. For tumor growth experiments, mice were randomized before being allocated to cages for treatment. All other experiments were nonrandomized and did not involve blinding of the investigators. In tumor growth experiments, variation is indicated using standard error of the mean; in cell culture experiments, variation is indicated using standard deviation. To assess statistical significance between two groups, a two-tailed Welch's unequal variances t-test was used. Where data showed a skewed distribution, a Wilcoxon signed-rank test was performed. To examine significance in xenograft between two groups, a two-way ANOVA followed by Tukey's multiple comparisons test was performed. Before applying an ANOVA, we first tested whether there was homogeneity of variation among the groups using the Brown-Forsythe test. RPM mice survival data were analyzed using log-rank (Mantel-Cox) test. In all figures, the p values were shown as: *, $p<0.05$; **, $p<0.01$; ***, $p<0.001$, ****, $p<0.0001$.

Cell Metabolism, Volume *28*

Supplemental Information

Inosine Monophosphate Dehydrogenase Dependence in a Subset of Small Cell Lung Cancers

Fang Huang, Min Ni, Milind D. Chalishazar, Kenneth E. Huffman, Jiyeon Kim, Ling Cai, Xiaolei Shi, Feng Cai, Lauren G. Zacharias, Abbie S. Ireland, Kailong Li, Wen Gu, Akash K. Kaushik, Xin Liu, Adi F. Gazdar, Trudy G. Oliver, John D. Minna, Zeping Hu, and Ralph J. DeBerardinis

Supplementary Figure 1. Related to Figure 1.

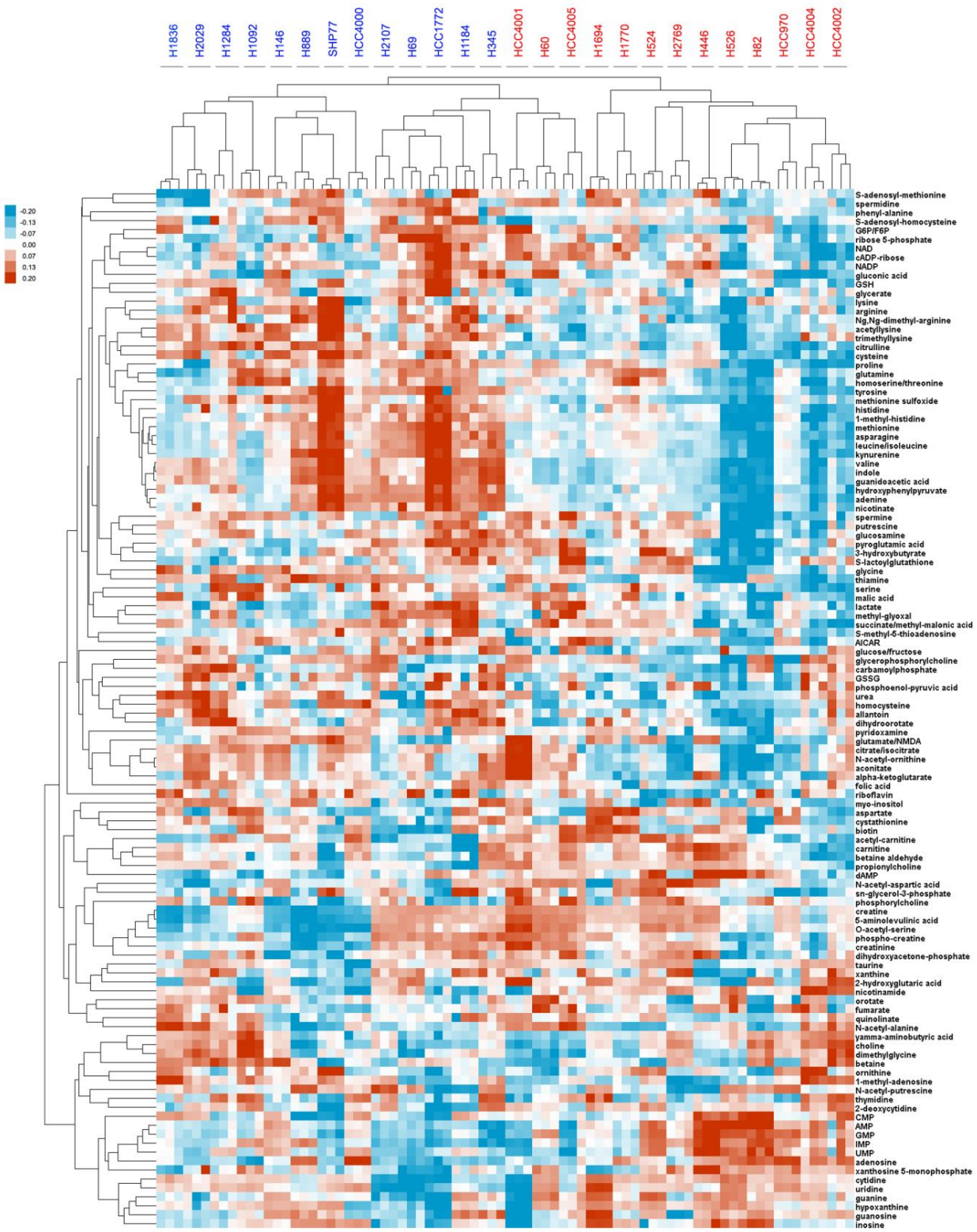

Supplementary Figure 2. Related to Figure 1.

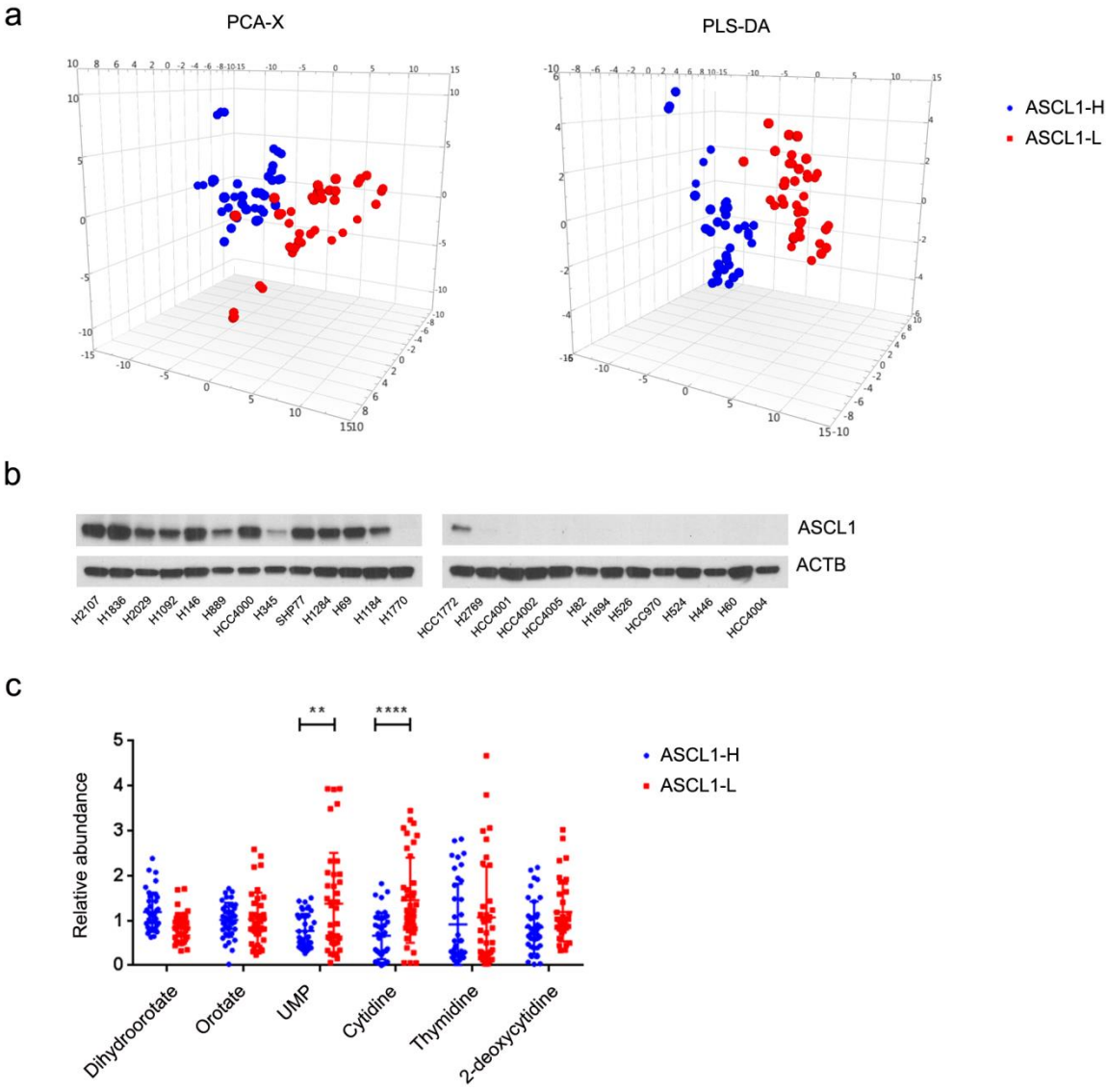

Supplementary Figure 3. Related to Figure 2.

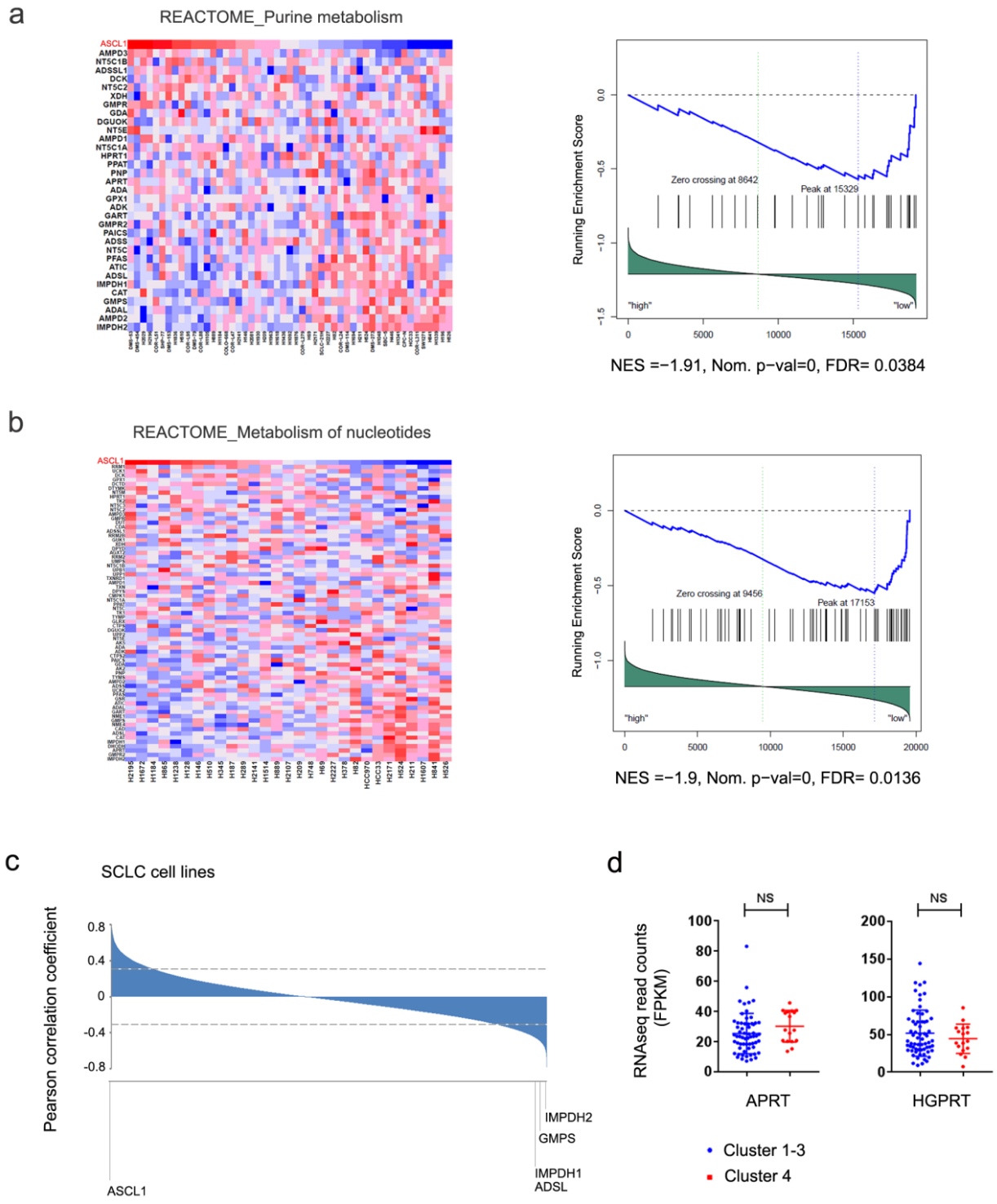

Supplementary Figure 4. Related to Figure 5.

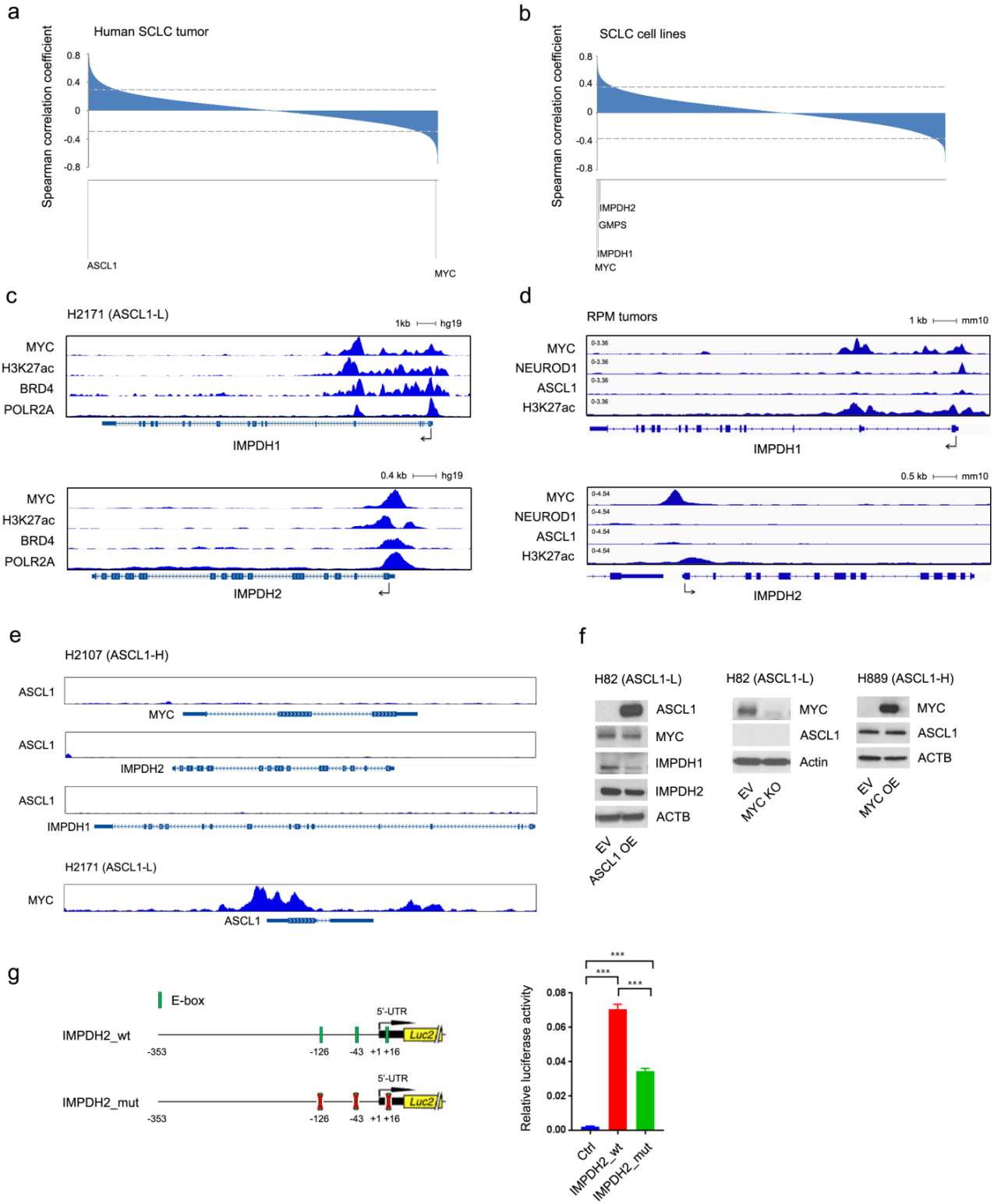

Supplementary Figure 5. Related to Figure 6.

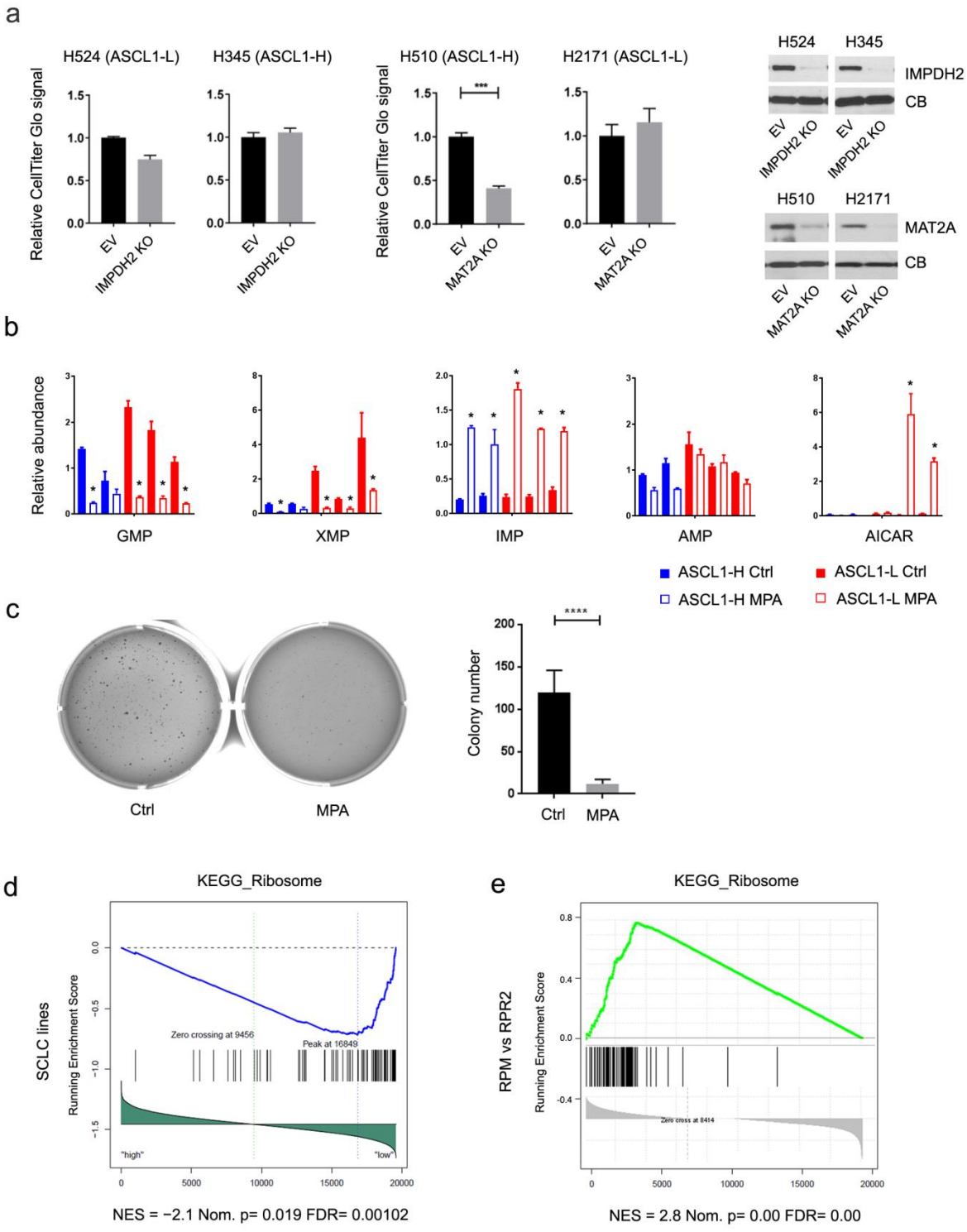

Supplementary Figure 6. Related to Figure 6.

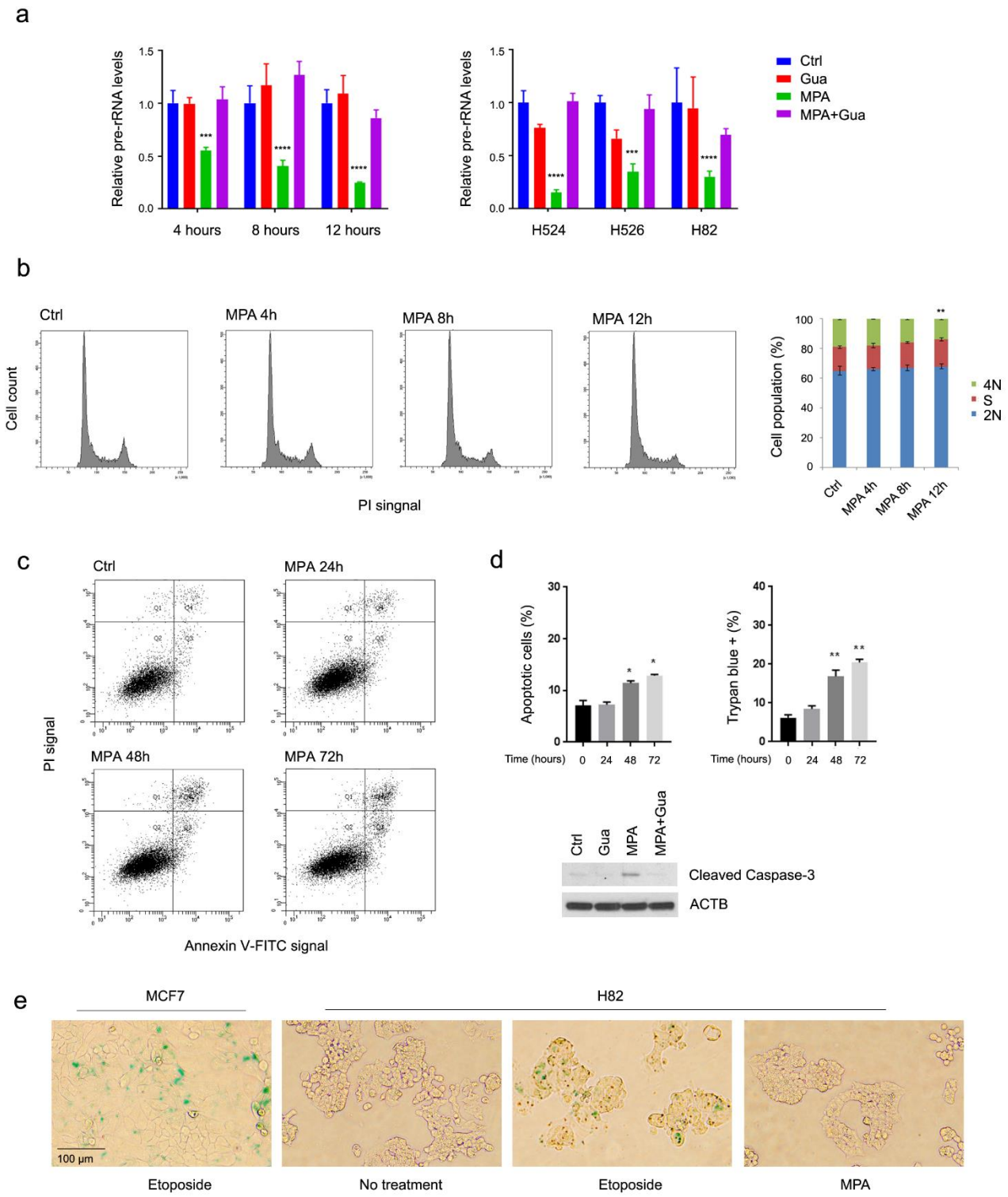

Supplementary Figure 7. Related to Figure 6.

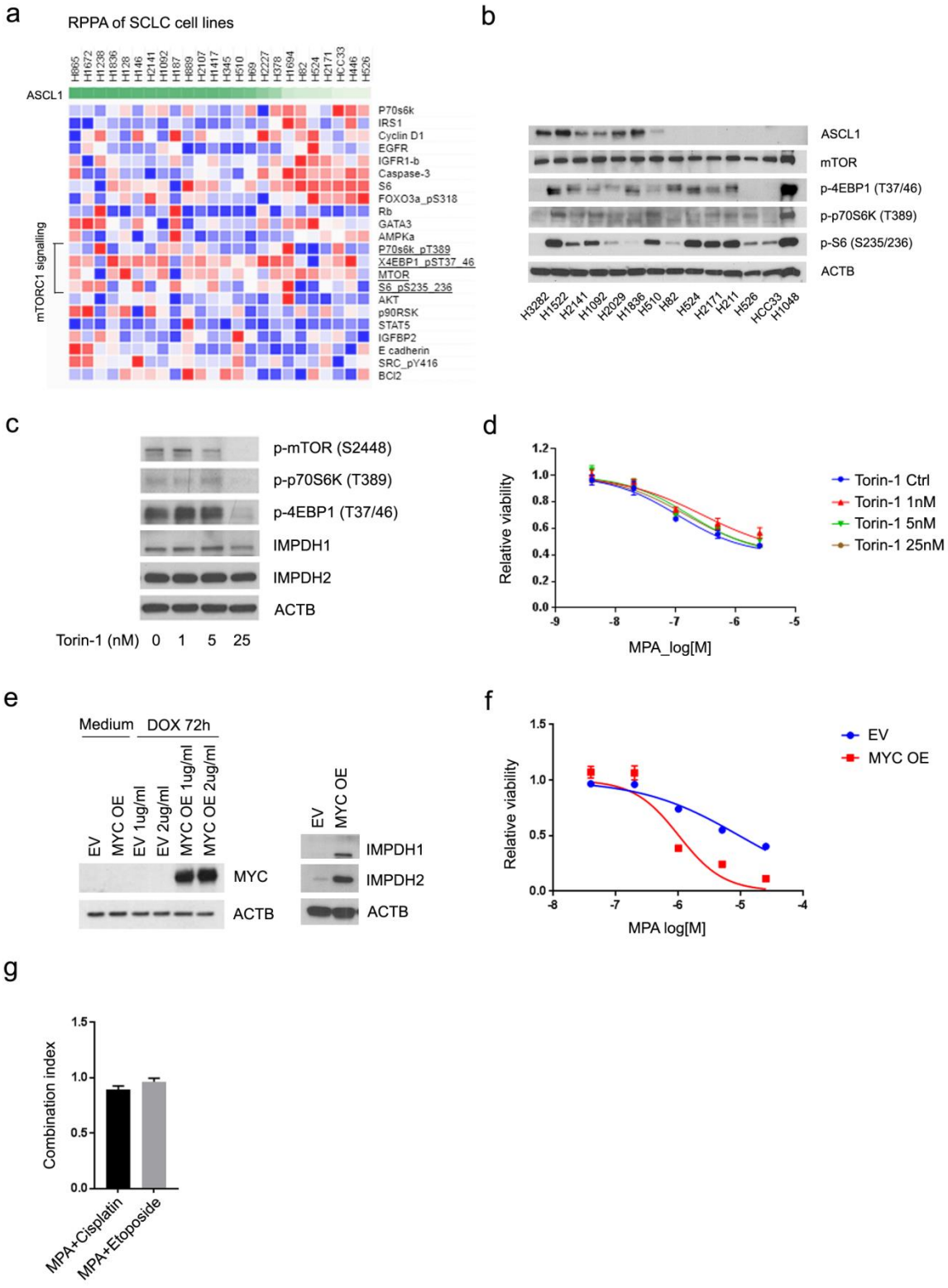

Supplementary Table 1. Oligonucleotides Sequences. Related to Key Resources Table.

Name	Sequences (5’-3’)
gRNA_MYC_forward	CACCGCTTCGGGGAGACAACGACGG
gRNA_MYC_reverse	AAACCCGTCGTTGTCTCCCCGAAGC
gRNA_IMPDH1_forward	CACCGGACGCCAAGGATTGAACTGG
gRNA_IMPDH1_reverse	AAACCCAGTTCAATCCTTGGCGTCC
gRNA_IMPDH2_forward	CACCGTGTGCTGTGAGTCCGTCGTC
gRNA_IMPDH2_reverse	AAACGACGACGGACTCACAGCACAC
gRNA_MAT2A_forward	CACCGCTTCCACGAGGCGTTCATCG
gRNA_MAT2A_reverse	AAACCGATGAACGCCTCGTGGAAGC
qPCR_ASCL1_forward	CCTGGTGCGAATGGACTT
qPCR_ASCL1_reverse	CAACGCCACTGACAAGAAAG
qPCR_MYC_forward	CTCGGATTCTCTGCTCTCCT
qPCR_MYC_reverse	TCTTGTTCCTCCTCAGAGTCG
qPCR_IMPDH1_forward	CAGCAGGTGTGACGTTGAAAG
qPCR_IMPDH1_reverse	AGCTCATCGCAATCATTGACG
qPCR_IMPDH2_forward	CTCCCTGGGTACATCGACTT
qPCR_IMPDH2_reverse	GCCTCTGTGACTGTGTCCAT
qPCR_ACTB_forward	AGAGCTACGAGCTGCCTGAC
qPCR_ACTB_reverse	AGCACTGTGTTGGCGTACAG
qPCR_pre-rRNA_forward	GCTCTACCTTACCTACCTGG
qPCR_pre-rRNA_reverse	TGAGCCATTCGCAGTTTCAC
qPCR_ATF4_forward	ATGACCGAAATGAGCTTCCTG
qPCR_ATF4_reverse	GCTGGAGAACCCATGAGGT
qPCR_E2F4_forward	CACCACCAAGTTCGTGTCCC
qPCR_E2F4_reverse	GCGTACAGCTAGGGTGTCA
qPCR_SDHB_forward	ACAGCTCCCCGTATCAAGAAA
qPCR_SDHB_reverse	GCATGATCTTCGGAAGGTCAA
qPCR_5S rRNA_forward	GGCCATACCACCCTGAACGC

qPCR_5S rRNA_reverse	CAGCACCCGGTATTCCCAGG
PCR_MYC-OE_forward	TTGGATCCATGCTGGATTTTTTTCGGGTAGTGG
PCR_MYC-OE_reverse	CCGCGGCCGCTTACGCACAAGAGTTCCGTAGCTGT

SUPPLEMENTARY FIGURE TITLES AND LEGENDS

Supplementary Figure 1. Related to Figure 1. Metabolomic profiling of SCLC cell lines. The heatmap shows **r**elative abundance of metabolites in 26 SCLC lines. The names of the cell lines at the top are coded according to ASCL1 status (blue, $ASCL1^{High}$; red, $ASCL1^{Low}$). Peak areas of each metabolite were normalized by total ion count. All replicates (3 independent cultures for each cell line) are included on the heatmap. Coloring on the heatmap reflects a $\log_2$ scale.

Supplementary Figure 2. Related to Figure 1. $ASCL1^{High}$ and $ASCL1^{Low}$ SCLC lines are metabolically distinct. a, Principal component analysis (unsupervised) and partial least squares discriminant analysis (supervised) of metabolomic signatures from 26 SCLC lines. The data used in this analysis are from the metabolomic analysis in **Supplementary Figure 1. b,** ASCL1 protein abundance in SCLC lines from panel **a**. **c,** Relative abundance of intermediates from pyrimidine metabolism in $ASCL1^{High}$ and $ASCL1^{Low}$ cell lines. Individual data points are shown along with mean abundance values and SD for three independent cultures of each line.

Supplementary Figure 3. Related to Figure 2. Genes involved in de novo purine biosynthesis are enriched in $ASCL1^{Low}$ SCLC. a, Gene set enrichment analysis reveals enrichment of the "Purine metabolism" gene set in $ASCL1^{Low}$ cell lines from the Cancer Cell Line Encyclopedia (CCLE) database (n=51 SCLC lines). The top row indicates abundance of *ASCL1* mRNA. **b,** Gene set enrichment analysis reveals enrichment of the "Metabolism of nucleotides" gene set in $ASCL1^{Low}$ cell lines from GSE32036 (n=29 SCLC lines). **c,** Pearson's correlation coefficients between abundance of *ASCL1* mRNA and all other transcripts from 51 SCLC lines in the CCLE database. Dashed lines demarcate p=0.05. **d,** Relative mRNA abundance of genes encoding the salvage enzymes *APRT* and *HGPRT* in clusters 1-3 versus cluster 4 in primary human tumors in **Figure 2 c,d**. Individual data points are shown along with mean and SD for each sample. NS, not significant.

Supplementary Figure 4. Related to Figure 5. MYC regulates de novo purine nucleotide synthesis in $ASCL1^{Low}$ SCLC. a, Spearman's correlation coefficients between abundance of *ASCL1* mRNA and all other transcripts in the 81 human SCLC tumors in **Figure 2d**. Dashed lines demarcate p=0.05. **b,** Spearman's correlation coefficients between abundance of *MYC* mRNA and all other transcripts in the 51 SCLC lines in **Supplementary Figure 3a**. Dashed lines

demarcate p=0.05. **c,** Chromatin signatures at the *IMPDH1* and *IMPDH2* loci in H2171 cells (ASCL1^{Low}). Chip-seq tracks of MYC, H3K27Ac, BRD4 and POLR2A are displayed. **d,** ChIP-Seq analysis of genomic binding at the *Impdh1* and *Impdh2* loci in RPM tumors for the indicated antibodies to MYC, NEUROD1, ASCL1 and H3K27ac. **e,** *Top,* ChIP-Seq of genomic ASCL1 binding at the *MYC, IMPDH1 and IMPDH2* loci in H2107 (ASCL1^{High}). *Bottom*, ChIP-Seq of genomic MYC binding at the *ASCL1* locus in H2171 (ASCL1^{Low}). **f,** *Left*, Abundance of MYC, ASCL1, IMPDH1 and IMPDH2 in H82 (ASCL1^{Low}) with ASCL1 overexpression or vector control. *Middle*, Abundance of MYC and ASCL1 in H82 (ASCL1^{Low}) with *MYC* knockout or vector control. *Right*, Abundance of MYC and ASCL1 in H889 (ASCL1^{High}) with doxycycline inducible MYC overexpression or vehicle. **g,** Luciferase assay with wild type (IMPDH2_wt) and E-box mutated (IMPDH2_mut) promoters of *IMPDH2* in H82 cells (ASCL1^{Low}). Data are represented as average and SD. ***p <0.001.

Supplementary Figure 5. Related to Figure 6. IMPDH is required for ASCL1^{Low} SCLC cell growth. a, Relative growth of several SCLC cell lines after CRISPR-Cas9-mediated knockout of *IMPDH2* or *MAT2A*. Data are represented as average and SD. ***p <0.001. Western blots are shown to verify loss of protein expression. **b,** Purine metabolite abundance in ASCL1^{High} (H345, H889) and ASCL1^{Low} (H524, H526, H82) cells treated with 1 μM MPA for 12 hours. Data are represented as average. *p < 0.05. **c,** Soft agar colony formation in H524 cells treated with vehicle or 1 μM MPA for two weeks. Data are represented as average and SD. ****p <0.0001. **d, e,** Gene set enrichment analysis reveals enhanced expression of genes involved in ribosome biogenesis in ASCL1^{Low} vs. ASCL1^{High} SCLC lines (GSE32036), and in RPM vs. RPR2 tumors (GSE89660).

Supplementary Figure 6. Related to Figure 6. IMPDH inhibition reduces ribosomal RNA transcription and induces apoptosis. a, qPCR for transcripts of pre-rRNA in H524 cells treated with vehicle or 1 μM MPA, with or without 50 μM guanosine for 4, 8 or 12 hours (*left*); and in three independent ASCL1^{Low} SCLC lines for 12 hours (*right*). Data are represented as average and SEM. ***p <0.001; ****p <0.0001. **b,** Propidium iodide staining of H524 cells treated with vehicle or 1 μM MPA for 4, 8, 12 hours. Data are represented as average and SD. **p <0.01. **c, d,** AnnexinV/Propidium iodide and trypan blue staining in H524 cells treated with vehicle or 1 μM MPA for 24, 48 and 72 hours. Data are represented as average and SD. *p < 0.05; **p <0.01. Abundance of cleaved Caspase-3 in H524 cells treated with vehicle or 1 μM MPA, with or without 50 μM guanosine for 48 hours. **e,** β-Gal staining in H82 cells

treated with vehicle, 5 μM Etoposide for 24 hours, or 1 μM MPA for 72 hours, and in MCF7 cells treated with 10 μM Etoposide for 24 hours. Scale bar, 100 μm.

Supplementary Figure 7. Related to Figure 6. IMPDH dependence in SCLC cells is dictated by MYC. a, Heatmap of protein abundance in 24 SCLC cell lines. Relevant proteins and phosphoproteins, including several from the mTORC1 pathway, are displayed. **b,** Abundance of ASCL1, p-4EBP1 (T37/46), p-p70S6K (T389) and p-S6 (S235/236) in 14 SCLC cell lines. **c,** Abundance of p-mTOR (S2448), p-4EBP1 (T37/46), p-p70S6K (T389), IMPDH1, IMPDH2 in H524 cells treated with vehicle or 1, 5, 25 nM Torin-1 for 24 hours. **d,** Dose response of H524 cells treated with MPA for 72 hours, and pretreated with vehicle or 1, 5, 25 nM Torin-1 for 24 hours. Data are represented as average and SD. **e,** *Left*, Abundance of MYC in H510 ($ASCL1^{High}$) with doxycycline inducible MYC overexpression or vehicle, with or without 1 or 2 μg/ml doxycycline treatment for 72 hours. *Right*, Abundance of IMPDH1 and IMPDH2 in H510 cells with doxycycline inducible MYC overexpression or vehicle. **f,** Dose response of H510 cells with doxycycline-inducible MYC overexpression or vehicle treated with MPA for 72 hours. MYC overexpression was induced by pre-treating with 1 μg/ml doxycycline for 72 hours. Data are represented as average and SD. **g,** Combination index in H524 cells treated with MPA plus cisplatin or etoposide for 72 hours. Data are represented as average and SD.